Nano Research

Open Access

Review Article

Electron microscopy in nanoparticle self-assembly research

Jun Chen[1], Chenyu Yan[2], Baixu Zhu[2], Chuanliang Huang[2], Fanrui Cheng[2], Hanyi Duan[2], and Xingchen Ye[2]✉

[1] *Electron Microscopy Center, Indiana University, Bloomington, Indiana 47405, USA*
[2] *Department of Chemistry, Indiana University, Bloomington, Indiana 47405, USA*

Cite this article: *Nano Research*, **2025**, *18*, 94907286. https://doi.org/10.26599/NR.2025.94907286

ABSTRACT: Nanoparticle self-assembly is a vital research field with significant implications for fundamental science and a wide range of technological applications. This bottom-up approach enables the design and fabrication of mesoscopic materials with distinct electronic, magnetic, optical, mechanical, and catalytic properties. Monodisperse nanoparticles serve as fundamental building blocks for creating long-range ordered structures known as superlattices, superstructures, or supercrystals. Advances in wet chemical synthesis methods have provided access to a variety of nanoparticle shapes, sizes, and compositions, establishing a solid foundation for extensive studies in self-assembly. This review highlights the utility and advantages of various electron microscopy methods for characterizing the structures and dynamics of nanoparticle assemblies, ranging from conventional imaging and diffraction techniques to cutting-edge approaches such as electron tomography, focused ion beam scanning electron microscopy tomography, four-dimensional scanning transmission electron microscopy, and liquid cell transmission electron microscopy. These methods enable the acquisition of detailed two-dimensional and three-dimensional structural information of nanoparticle superlattices in dry, frozen, and liquid states. We also highlight the development of advanced data processing algorithms and their implementation in open-source software packages to facilitate electron microscopy data analysis. By leveraging machine learning techniques, researchers can efficiently manage large and complex electron microscopy datasets and gain deeper insights into the mechanisms of nanoparticle self-assembly. We anticipate that the comprehensive electron microscopy toolkit, combined with advanced computational algorithms and machine learning, will continue to generate new knowledge and insights in nanoparticle self-assembly research.

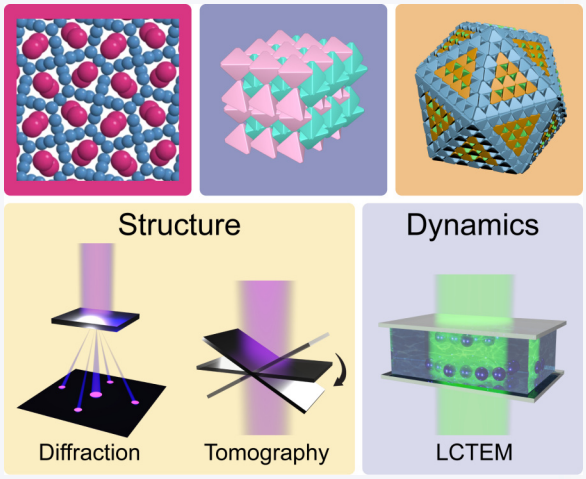

KEYWORDS: nanoparticle self-assembly, nanoparticle superlattices, electron microscopy, imaging, diffraction, tomography, liquid cell transmission electron microscopy

1 Introduction

Nanoparticle self-assembly is of great interest for advancing both fundamental research and a wide range of technological applications [1, 2]. This bottom-up approach offers a versatile pathway for fabricating mesoscopic and macroscopic materials with emergent electronic, mechanical, magnetic, optical, and catalytic properties [3–9]. Monodisperse nanoparticles serve as fundamental nanoscale building blocks for creating long-range ordered arrays, often referred to as nanoparticle superlattices, supercrystals, or superstructures. Advances in wet chemical methods over the past three decades have facilitated the reliable synthesis of monodisperse nanoparticles with diverse sizes, shapes, compositions, and functionalities, creating a comprehensive library for self-assembly studies [10–17]. The three key experimental parameters for nanoparticle self-assembly are the characteristics of the hard inorganic cores, the soft organic surface ligands, and the assembly methods or conditions. Pristine surface ligands allow the as-synthesized nanoparticles to be well-dispersed in either nonpolar or polar solvents, providing steric or electrostatic stabilization. Typical short-chain alkyl ligands on the nanoparticle surfaces can be chemically exchanged for other types of ligands. Various types of ligands can be grafted onto nanoparticle surfaces through ligand exchange, including polymer brushes, dendrimer ligands, DNA,

Received: November 14, 2024; **Revised:** February 1, 2025
Accepted: February 6, 2025

✉Address correspondence to xingye@indiana.edu

and charged small molecules. These non-native ligands can regulate interparticle interactions and shift the self-assembly mechanism from entropy-driven to enthalpy-driven. Consequently, structurally distinct nanoparticle superlattices can be self-assembled from the same nanoparticle cores by employing different surface ligands. Various methods for nanoparticle self-assembly have been developed, which can be broadly categorized into two main types: drying-mediated self-assembly and non-drying mediated self-assembly. In drying-mediated self-assembly, nanoparticle superlattices are formed by the gradual evaporation of nanoparticle solutions on solid substrates, liquid subphases, or within liquid emulsion droplets. This method has been utilized for nanoparticles capped with native ligands [18, 19], polymeric ligands [20–22] and dendrimer ligands [23, 24]. On the other hand, in non-drying mediated self-assembly, the nucleation and growth of nanoparticle superlattices in solution can be initiated by adjusting various parameters, such as pH, ionic strength, temperature, and polarity. This method has been employed for nanoparticles capped with DNA ligands [25–27], charged small molecules [28–30], polymeric ligands [31–33], dendrimer ligands [34, 35], and native ligands [36].

Structural characterization of nanoparticle superlattices is essential for understanding the self-assembly mechanisms and structure–property relationships. Electron microscopy is a powerful characterization tool due to its high spatial resolution and diverse analytical modalities, including imaging, diffraction, and spectroscopy. It provides structural information in both real space and reciprocal space across a broad range of length scales, from micrometers to sub-nanometers [37–39]. The rapid advancement of electron microscopy instrumentation, including high-performance detectors, microfabricated liquid cells, and specialized sample holders, allows for the visualization of both static structures and the dynamic processes of nanoparticle self-assembly. Concurrently, advancements in computational algorithms, open-source software, and machine learning facilitate the efficient acquisition, processing, and analysis of large datasets generated by multimodal electron microscopy experiments.

This review focuses on the various electron microscopy techniques used in nanoparticle self-assembly research. We will first discuss how transmission electron microscopy (TEM) imaging and diffraction, along with scanning electron microscopy (SEM) imaging, have been routinely utilized to identify the structures of various nanoparticle superlattices. Next, we will assess the utility of electron tomography and focused ion beam scanning transmission electron microscopy (FIB-SEM) tomography, conducted at both room and cryogenic temperatures, for resolving the three-dimensional (3D) structures of complex nanoparticle superlattices. Finally, we will discuss the advantages of recently developed electron microscopy techniques, such as four-dimensional scanning transmission electron microscopy (4D-STEM), fast electron tomography, and liquid cell transmission electron microscopy (LCTEM), as well as the new insights they provide into the structure and dynamics of nanoparticle self-assembly.

2 Electron microscopy characterization of static nanoparticle assemblies

2.1 Electron microscopy imaging and diffraction of nanoparticle assemblies

Conventional electron microscopy techniques, including TEM imaging, small-angle electron diffraction (SAED), wide-angle electron diffraction (WAED), and SEM imaging, have been extensively utilized to investigate the structures of various nanoparticle assemblies [40–53]. Spherical nanoparticles are frequently regarded as atomic analogs because they can self-assemble into superlattices that mirror the structural arrangements found in atomic solids. In a groundbreaking 1995 study, Murray et al. combined TEM imaging, SAED, and SEM imaging (Figs. 1(a) and 1(b)) to investigate the face-centered cubic (FCC) structure and morphology of superlattices self-assembled from CdSe quantum dots [18]. Later, Shevchenko et al. reported over fifteen distinct binary nanoparticle superlattice (BNSL) structures such as NaCl, CuAu, CsCl, AlB_2, $MgZn_2$, $MgNi_2$, Cu_3Au, Fe_4C, $CaCu_5$, CaB_6, and $NaZn_{13}$, self-assembled from many combinations of semiconducting, metallic, and magnetic nanoparticles (Figs. 1(d)–1(i)) [19]. Talapin et al. discovered the first dodecagonal quasicrystalline (DDQC) BNSLs (Fig. 1(c)) self-assembled from multiple combinations of nanoparticles [40]. Later, Ye et al. reported a different type of DDQC BNSLs coexisting with the σ phase (Fig. 1(l)) [54]. In shape-anisotropic nanoparticle self-assembly, TEM and SEM imagings enable visualization of particle shape and arrangement in real space, while SAED and WAED provide insights into lattice symmetry and particle orientation through reciprocal space analysis. For example, the TEM imaging, SAED, and WAED conducted by Ye et al. (Figs. 1(k) and 1(l)) revealed parallel arrangements of DyF_3 rhombohedral nanoplates and alternating arrangements of DyF_3 hexagonal nanoplates in the self-assembled two-dimensional (2D) superlattices [44]. SEM imaging by Henzi et al. (Figs. 2(a)–2(c)) revealed supercrystals self-assembled from Ag cubes, truncated octahedra, and octahedra exhibiting densest lattice packings [42]. Using SEM imaging, Wang et al. observed multiply twinned supracrystals self-assembled from Au tetrahedral nanocrystals, adopting both icosahedral and hexagonal plate-like shapes (Figs. 2(d)–2(k)) [53]. For most thin nanoparticle superlattices (< 300 nm thick), acquiring TEM images and corresponding SAED patterns along characteristic zone axes, then comparing them with modeled crystal structures, is often sufficient for accurate structural assignment. When 2D projections of different structures appear highly similar, structural misassignment of nanoparticle superlattices may occur due to limited structural information from the same superlattice domain. This challenge can be addressed by TEM tilting methods, which provide additional 2D projections and SAED patterns from the same domain by tilting the specimen to various orientations. Structural assignment of nanoparticle superlattices involves matching 2D projections and SAED patterns from the same domain, captured at various tilt angles, to a crystal model. This process requires only a standard TEM specimen mounted on a single- or double-tilt holder. Tilting is paused upon observing a clear projection from a new zone axis, allowing for the acquisition of corresponding TEM image and SAED pattern.

The TEM tilting method has been used to distinguish the structures of BNSLs with polymorphic phases. For example, Chen et al. employed a 3D crystallographic approach using a dual-axis tomography TEM holder to systematically characterize the structure of AB_{13}-type BNSLs, for which two polymorphs—ico-AB_{13} and cub-AB_{13}—had been proposed (Figs. 3(a)–3(d)) [55]. The tomography holder's in-plane 360° rotation capability enables alignment of a specific crystallographic direction parallel to the tilt axis prior to tilting. The crystallographic tool of stereographic projection is used to design series tilt paths. A total of nine tilt series were acquired and 14 distinct crystallographic projections of the

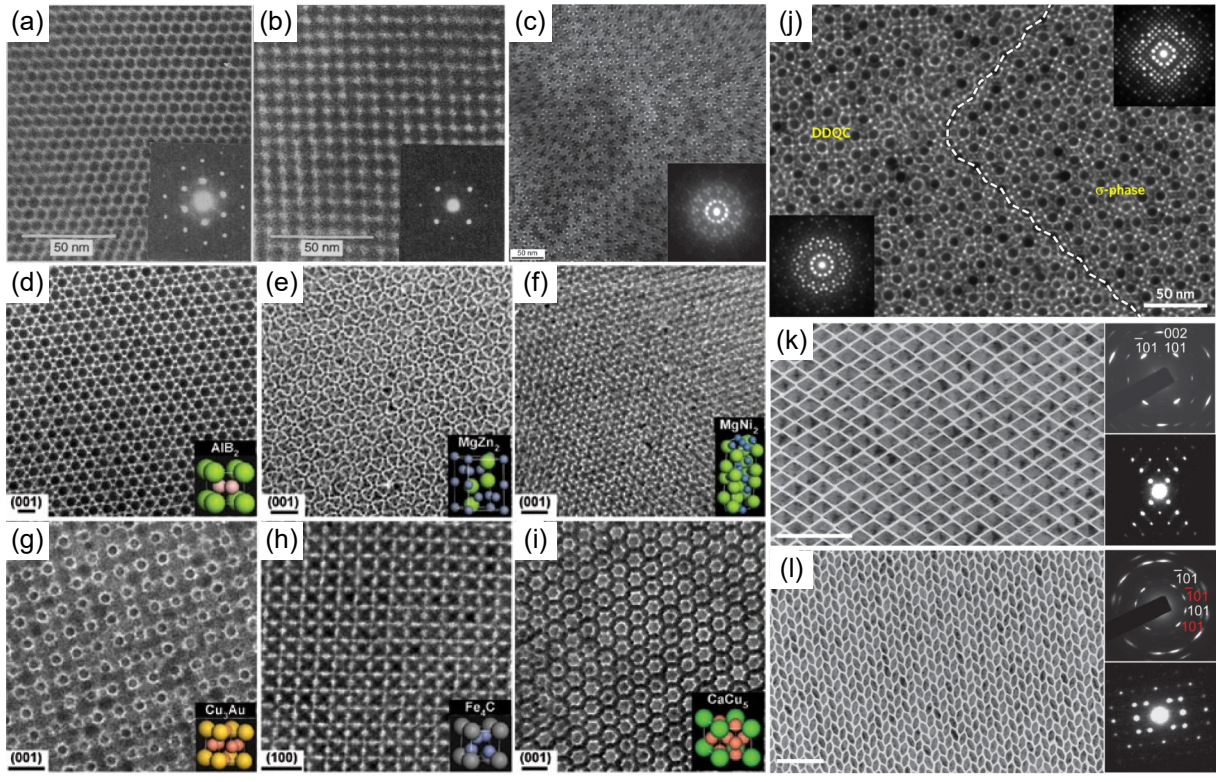

Figure 1 TEM images and electron diffraction patterns of single component and binary nanoparticle superlattices. (a) and (b) TEM images and SAED patterns (insets) of [101] and [100] projections of fcc superlattices self-assembled from 4.8 nm CdSe quantum dots. Reproduced with permission from Ref. [18], © American Association for the Advancement of Science 1995. (c) TEM image and SAED pattern (inset) of a dodecagonal quasicrystalline superlattice self-assembled from 13.4 nm Fe_2O_3 and 5 nm Au nanoparticles. Reproduced with permission from Ref. [40], © Macmillan Publishers Limited 2009. (d)–(i) TEM images of the characteristic projections of binary superlattices self-assembled from (d) 6.7 nm PbS and 3.0 nm Pd, (e) 6.2 nm PbSe and 3.0 nm Pd, (f) 5.8 nm PbSe and 3.0 nm Pd, (g) 7.2 nm PbSe and 4.2 nm Ag, (h) 6.2 nm PbSe and 3.0 nm Pd, and (i) 7.2 nm PbSe and 5.0 nm Au nanoparticles. The insets show the superlattice projections (left bottom) and the corresponding three-dimensional structures (right bottom). Reproduced with permission from Ref. [19], © Nature Publishing Group 2006. (j) TEM image of the phase boundary between the dodecagonal quasicrystal and σ phase self-assembled from 12.0 nm Fe_3O_4 and 6.8 nm $CoFe_2O_4$ nanoparticles. Insets show the corresponding SAED patterns of the DDQC (left bottom) and σ phase (right bottom), respectively. Reproduced with permission from Ref. [54], © Macmillan Publishers Limited, part of Springer Nature 2016. (k) and (l) TEM images (left), wide-angle and small-angle (upper right and lower right) electron diffraction patterns of superlattices self-assembled from DyF_3 rhombohedral nanoplates and hexagonal nanoplates, respectively. Reproduced with permission from Ref. [44], © Macmillan Publishers Limited 2013. Scale bars: ((d), (g), and (h)) 10 nm, ((e), (f), and (i)) 20 nm, and ((k) and (l)) 100 nm.

AB_{13}-type BNSLs were identified. All TEM images and corresponding SAED patterns from each tilt series confirm the phase-pure ico-AB_{13}-type BNSLs self-assembled from various combinations of oleic acid-capped Fe_3O_4 nanocrystals. Using the TEM tilting technique, Ye et al. identified a new AB_6 polymorph with body-centered cubic (bcc) symmetry in Au-Fe_3O_4 BNSL, distinct from the previously known simple cubic CaB_6 phase [56]. The TEM tilting experiments conducted by Bodnarchuk et al. allowed for the differentiation between (100) projections of AlB_2-type and (010) projections of CuAu-type BNSLs, as well as between (001) projections of CuAu-type and (001) projections of CsCl-type BNSLs composed of either 3.4 or 4.9 nm dodecanethiol-capped Pd nanocrystals and oleic acid-capped 7.7 nm PbSe nanocrystals [57].

TEM tilting methods were also used to determine the structure of shape-anisotropic nanoparticle superlattices. For example, Boles et al. conducted TEM tilting experiments on superlattices self-assembled from zinc-blend CdSe nanotetrahedra with 8 or 10 nm edge lengths, capped with oleic or stearic acid ligands (Figs. 3(e)–3(h)) [58]. The results confirmed that the three characteristic projections from different domains correspond to the same superlattice structure. The unit cell of the superlattice comprises two tetrahedra oriented in opposite directions, featuring a center of inversion. Nagaoka et al. used TEM tilting to characterize the bcc superlattice self-assembled from wurtzite CdSe/CdS core–shell nanotetrahedra with an effective edge length of 10.3 nm. The bottom facet of the nanotetrahedra is coated with octadecylphosphonic acid, while the three equivalent side facets are coated with oleic acid [59].

2.2 Electron tomography for resolving the 3D structure of nanoparticle assemblies

While TEM imaging and tilting techniques have aided in determining the structures of many nanoparticle superlattices, they are insufficient for resolving the complete 3D structure of complex nanoparticle assemblies. Electron tomography is the technique of choice for 3D structural characterization of complex nanoparticle assemblies, as it enables the visualization of individual nanoparticles within superlattices at nanometer resolution across a wide field of view [54, 60–72]. Electron tomography consists of three stages: data acquisition, alignment, and reconstruction. A single-axis high tilt holder is used to acquire a series of projection images across a wide angular range (e.g., ±60° and ±70°) with small increments (e.g., 1° and 2°). This extensive tilt range is necessary to minimize the missing wedge problem, which occurs due to missing information in uncovered tilt angles and can cause elongation of reconstructed

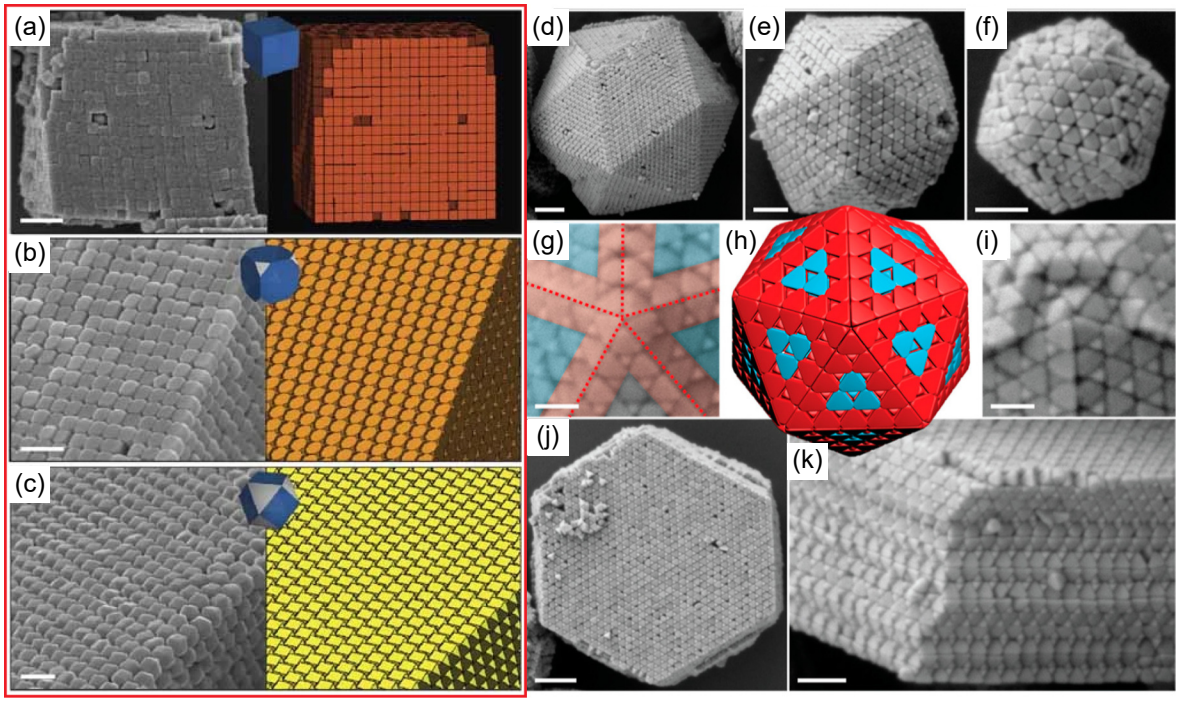

Figure 2 SEM images of anisotropic nanoparticle supercrystals. (a)–(c) SEM images of supercrystals self-assembled Ag cubes (a), truncated cubes (b), and truncated octahedra (c) with edge lengths of 122, 68, and 106 nm, respectively. Reproduced with permission from Ref. [42], © Macmillan Publishers Limited 2012. (d)–(k) SEM images of icosahedral-shaped (d)–(i) and hexagonal plate-shaped (j) and (k) supercrystals self-assembled from Au tetrahedra with edge length of 48 nm. Reproduced with permission from Ref. [53], © American Chemical Society 2022. Scale bars: ((a)–(c)) 500 nm, ((d), (j), and (k)) 200 nm, ((e) and (f)) 100 nm and ((g) and (i)) 50 nm.

nanoparticles in the direction perpendicular to the tilting axis [73]. A specialized tomography holder with in-plane rotation allows for the acquisition of two orthogonal tilt series of projection images from the same nanoparticle superlattices, improving reconstruction quality by reducing the missing wedge to a missing pyramid [74]. Due to sample drift during tilting experiments, the acquired tilt series must be aligned to correct drifts among projection images recorded at different tilt angles. Alignment algorithms use either the coordinates of a few fiducial markers, whole image cross correlation, or patched image cross correlation at different tilt angles. Several free software packages, including IMOD [75], ASTRA [76], and Tomviz [77], have been developed to implement various reconstruction algorithms, such as weighted back projection (WBP) and simultaneous iterative reconstruction techniques (SIRT) [78]. WBP is a non-iterative method that determines the Fourier transform of the object from the Fourier transforms of the measured projections and uses a weighting filter in the Fourier space to correct the uneven sampling of spatial frequencies before back projection to obtain the 3D structure of the object. In contrast, SIRT is an iterative real space method that iteratively refines the reconstructed 3D volume by minimizing the deviation between re-projections from the reconstructed 3D volume and the measured projections of the object. WBP is a fast reconstruction algorithm and often used as the routine reconstruction method for big datasets with a wide range of tilting angles and large number of projections, while SIRT is more computationally demanding but has the advantage of reduced reconstruction artifacts for datasets with a narrow range of tilting angles and small number of projections [73].

Electron tomography can be conducted in either bright-field TEM (BF-TEM) or high-angle annular dark-field scanning transmission electron microscopy (HAADF-STEM) modes. BF-TEM is primarily used for samples with minimal diffraction contrast, while HAADF-STEM is better suited for samples with high diffraction contrast. Both BF-TEM and HAADF-STEM tomography have been used to characterize the 3D structure of complex nanoparticle assemblies, allowing clear visualization of nanoparticle types, positions, and orientations. For example, Evers et al. used BF-TEM tomography to examine the 3D structure of a ternary nanoparticle superlattice formed on TEM grids by slowly evaporating toluene from mixed ternary nanocrystal suspensions at 70 °C under reduced pressure [60]. Electron tomography reconstruction revealed that the ABC_4-type ternary nanoparticle superlattice is isostructural with the $AlMgB_4$ atomic lattice, with 12.1 and 17.9 nm PbSe nanocrystals occupying the A and B positions, and 5.8 nm CdSe nanocrystals located at C sites (Figs. 4(a)–4(h)). Boneschanscher et al. used BF-TEM tomography to determine the 3D structure of an A_6B_{19}-type binary BNSL assembled from 6.5 nm PbSe and 3.4 nm CdSe nanocrystals with a size ratio of 0.67 [66]. The reconstruction revealed that the A_6B_{19}-type BNSL comprises stacked layers forming a Kagome-like lattice of PbSe nanocrystals, with CdSe nanocrystals occupying the interstitial sites (Figs. 4(i)–4(m)).

Ye et al. used BF-TEM tomography to investigate the 3D structure of a novel DDQC BNSL thin film, formed by slow drying of binary nanocrystal mixtures in hexane on an immiscible diethylene glycol subphase [54]. The SAED patterns display sharp diffraction spots with 12-fold rotational symmetry, while the TEM images reveal the characteristic square-triangle tiling of the DDQC structure and an absence of translational periodicity (Fig. 4(n)). Electron tomography was used to resolve the 3D structure and identify the types and positions of individual nanocrystals within layers of the DDQC BNSLs. The reconstruction revealed that while the overall structure exhibits 12-fold symmetry, each sublayer

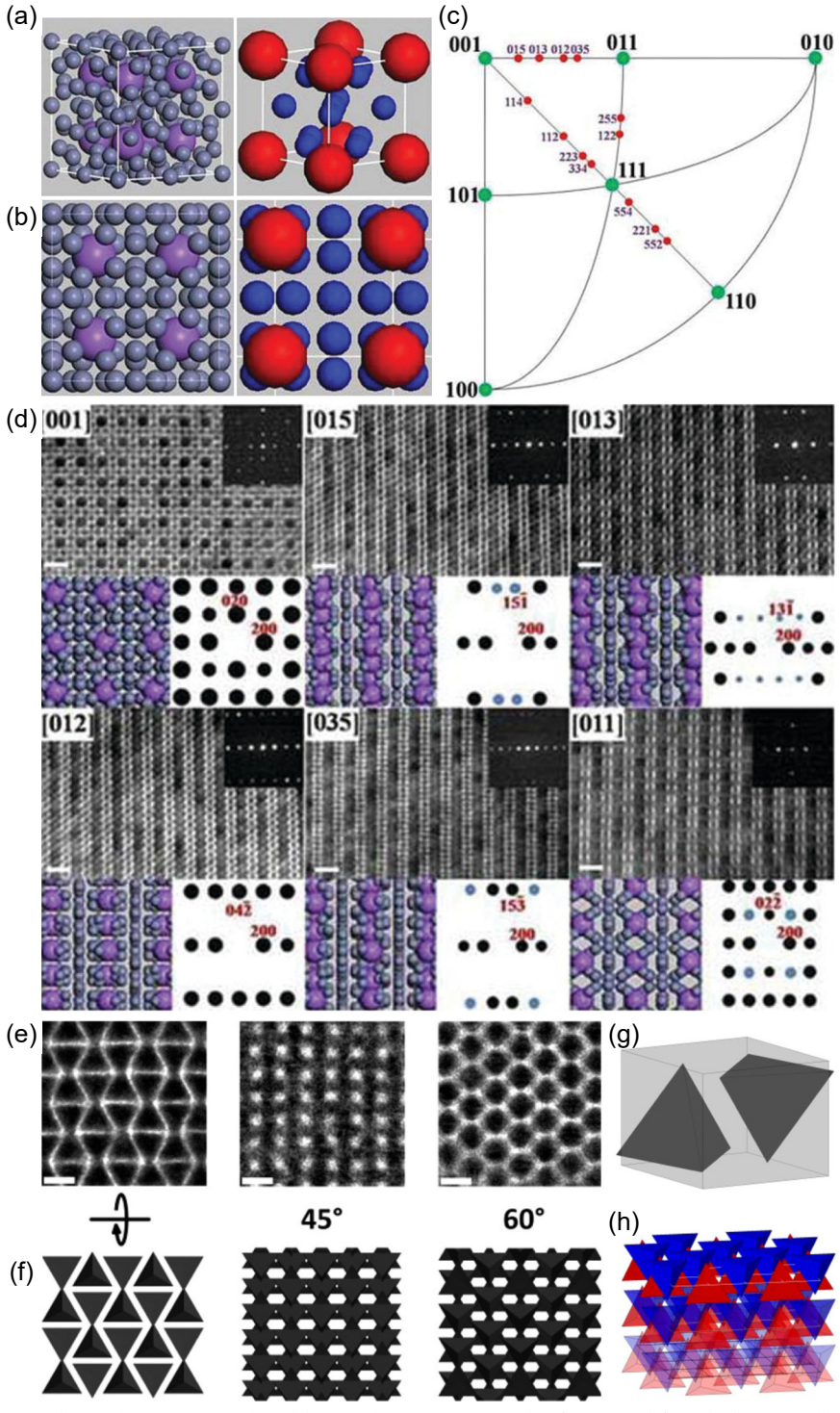

Figure 3 Series tilting of nanoparticle superlattices. Structural models (a) and [001] projections (b) of ico-AB_{13} (left) and cub-AB_{13} (right) structures. (c) Stereographic projection of the cubic crystal system. (d) A tilt series of ico-AB_{13} binary superlattices self-assembled from 10.5 and 5.6 nm Fe_3O_4 nanoparticles. Below each TEM image (inset shows the SAED pattern) are the projections from structural models and simulated SAED pattern. Tilting sequence: [001]→[015]→[013]→[012]→[035]→[011] zone axes. Reproduced with permission from Ref. [55], © American Chemical Society 2010. (e)–(h) A tilt series of TEM images (e), corresponding modeled projections (f), unit cell (g), and structural model (h) of superlattices self-assembled from CdSe tetrahedra with 10-nm edge length. Reproduced with permission from Ref. [58], © American Chemical Society 2014. Scale bars: (d) 20 nm and (e) 10 nm.

shows a reduced 6-fold symmetry (Fig. 4(o)). The 6-fold symmetric layers rotate by 30° between the non-primed (P, M) and primed (P', M') layers, confirming the presence of screw symmetry. Tomographic reconstruction further reveals that the M layers comprise rectangles and equilateral triangles of two distinct edge lengths, with the rectangle's edges matching those of the small and large triangles. High-resolution SEM images revealed the rectangle–large triangle–small triangle tiling in the surface topography of DDQC BNSLs. This structure was observed across four binary nanocrystal systems: 6.8 nm $CoFe_2O_4$ with 12.0 nm

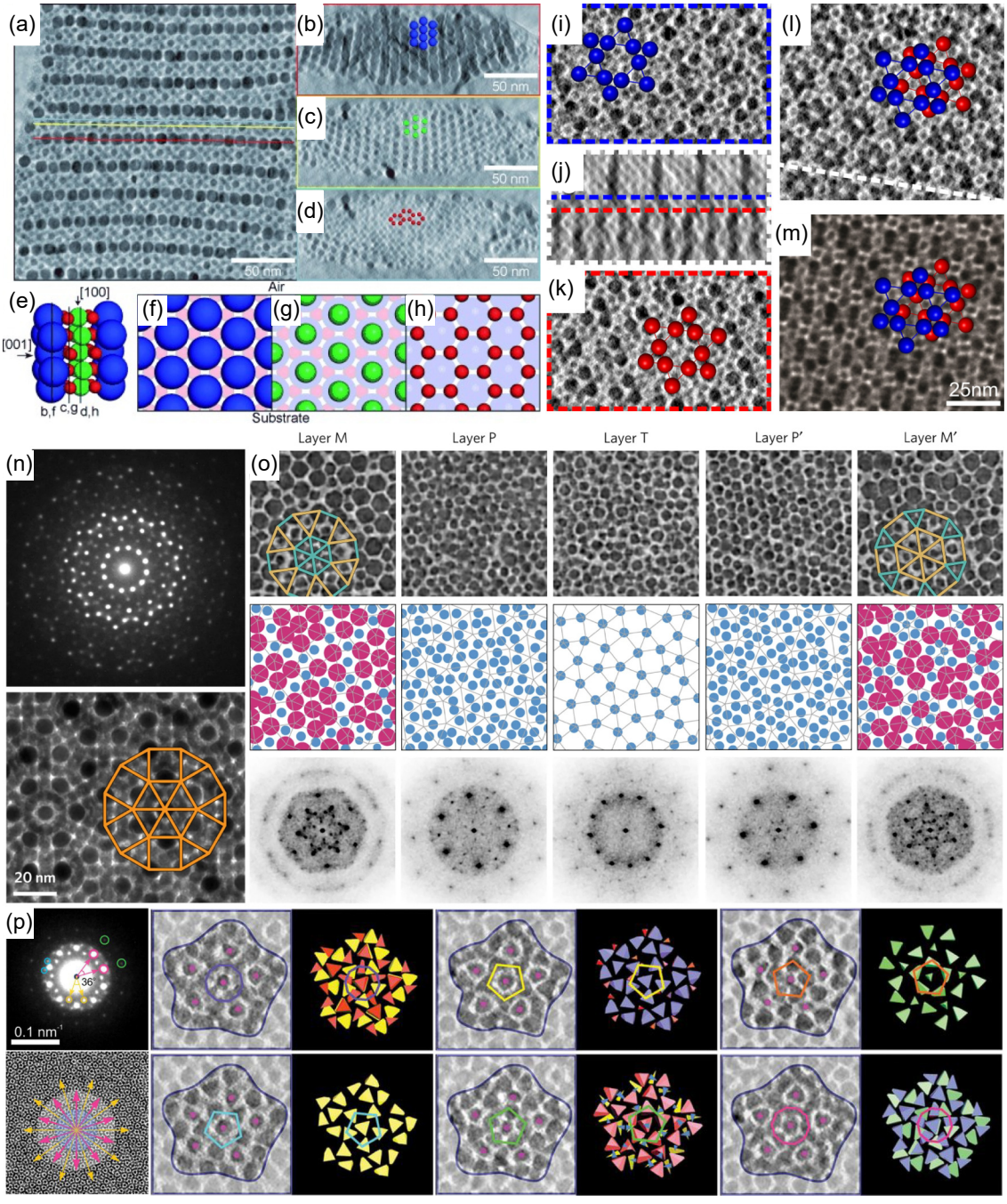

Figure 4 Electron tomography of nanoparticle superlattices. (a)–(h) Slice views of electron tomography reconstruction (a)–(d) and the corresponding structural models (e)–(h) of the ABC_4-type ternary nanoparticle superlattices self-assembled from 12.1 and 17.1 nm PbSe and 5.8 nm CdSe nanocrystals. Reproduced with permission from Ref. [60], © Wiley-VCH Verlag GmbH & Co. KGaA, Weinheim 2009. (i)–(m) Slice views of electron tomography reconstruction (i)–(l) and TEM image (m) of A6B19 binary superlattices self-assembled from 6.5 nm PbSe and 3.4 nm CdSe nanocrystals. Reproduced with permission from Ref. [66], © American Chemical Society 2013. (n) SAED pattern (top) and TEM image (bottom), (o) slice views of electron tomography reconstruction (top), corresponding structural models (middle) and fast Fourier transform patterns (bottom) of a dodecagonal quasicrystalline binary superlattice self-assembled from 6.8 nm $CoFe_2O_4$ and 12.0 nm Fe_3O_4 nanocrystals. Reproduced with permission from Ref. [54], © Macmillan Publishers Limited, part of Springer Nature 2016. (p) SAED pattern (left top), TEM image (left bottom), and slice views of electron tomography reconstruction of a decagonal quasicrystalline superlattice self-assembled from CdSe/CdS core–shell nanocrystals with height of 6.7 nm. Reproduced with permission from Ref. [69], © American Association for the Advancement of Science 2018.

Fe_3O_4, 6.2 nm FePt with 11.5 nm Fe_3O_4, 5.8 nm Au with 9.7 nm Fe_3O_4, and 8.8 nm Fe_3O_4 with 14.6 nm Fe_3O_4. These observations demonstrate that the formation of DDQC BNSLs is robust and essentially independent of the chemical composition of the constituent nanocrystals. In all combinations, the nanocrystal size ratio falls within the range of 0.60–0.66, calculated based on effective sizes that include both the inorganic core and the ligand shell. Molecular dynamics simulations suggest that the particle size ratio and the width of the attractive potential well are key factors in stabilizing the DDQC phase over competing structures.

Using BF-TEM tomography, Nagaoka et al. resolved the 3D structure of a novel single-component decagonal quasicrystalline

superlattice [69]. This superlattice comprises truncated tetrahedral wurtzite CdSe/CdS core–shell quantum dots (TTQDs) with heights of 6.7 or 8.5 nm, featuring three oleic acid-capped facets and one facet coated with octadecylphosphoric acid. The decagonal quasicrystalline superlattices were assembled by the slow evaporation of a cyclohexane solution containing TTQDs on an ethylene glycol liquid subphase. TEM images reveal the absence of translational periodicity, while SAED patterns display 10-fold rotational symmetry, confirming the decagonal quasicrystalline ordering (Fig. 4(p)). Electron tomography was used to elucidate the 3D TTQC packing within the decagonal quasicrystalline superlattices. The reconstruction revealed a consistent 10-fold rotational symmetry across all slices, along with a distinctive alternating pentagon–decagon–pentagon pattern from top to bottom slices (Fig. 4(p)). The shape of the TTQDs, combined with the anisotropic surface patchiness from the two distinct capping ligands, was found to be crucial for the formation of the decagonal quasicrystalline superlattices.

Electron tomography has also been utilized to investigate the 3D structure of nanocrystal supraparticles assembled within emulsion droplet templates. For example, Wang et al. employed HAADF-STEM tomography to examine the 3D structure of binary icosahedral supraparticles, which were assembled through the slow drying of emulsion droplets created by mixing a cyclohexane nanocrystal dispersion with an aqueous solution of dextran and sodium dodecyl sulfate [79]. The binary icosahedral supraparticles consist of 7.7 nm CdSe and 9.9 nm PbSe nanocrystals with an effective size ratio of 0.78 and a 2:1 number ratio of small to large nanocrystals. This same binary combination forms an $MgZn_2$ Laves phase when the cyclohexane solution of nanocrystals was slowly dried on a diethylene glycol surface, indicating that the $MgZn_2$ phase is the bulk-stable structure. Electron tomography was conducted to analyze the 3D structure of six supraparticles with diameters of 80, 110, 132, 167, 170, and 187 nm. Using an advanced tomographic reconstruction algorithm, the coordinates of all particles were successfully retrieved. The reconstruction revealed binary icosahedral clusters in all supraparticles, consisting of tetrahedral domains with a cubic $MgCu_2$-like structure and exhibiting five-fold symmetry. Both experimental results and simulations indicate that the formation of binary icosahedral supraparticles is driven by spherical confinement. Additionally, electron tomography has been used to characterize the 3D structure of supraparticles composed of shape-anisotropic nanoparticles [80] and polymer-grafted nanoparticles [81], revealing core–shell structures resulting from spherical confinement and/or the minimization of liquid/liquid interfacial energy.

2.3 FIB-SEM tomography to uncover the 3D structure of nanoparticle assemblies

TEM tomography is typically restricted to nanoparticle assemblies with a thickness of less than 300 nm, as the quality of the reconstruction deteriorates for thicker samples due to the limited penetration of the electron beam. In contrast, FIB-SEM tomography is well-suited for 3D structural characterization of thick nanoparticle assemblies, thanks to its different volume generation mechanism [82–85]. FIB-SEM tomography is performed using a dual-platform FIB-SEM microscope, where synchronized FIB milling removes thin slices, and SEM imaging captures the newly exposed cross-sections. This process allows for the acquisition of sequential stacks of SEM images. Following post-acquisition image processing steps such as denoising and alignment to correct for sample drift during data collection, the 3D volume data is generated directly from the aligned stacks of SEM images. The resolution of FIB-SEM tomography can reach 2–3 nm, typically determined by the minimum thickness of each milled slice. While FIB-SEM tomography requires substantially longer data acquisition times than TEM tomography, the sequential FIB milling and SEM imaging process is fully automated in modern FIB-SEM microscopes.

FIB-SEM tomography has been employed to uncover the 3D structure of large supercrystals self-assembled from anisotropic nanoparticles, such as Au nanorods [83, 84] and Au nanotetrahedra [85]. For instance, Wang et al. utilized FIB-SEM tomography to examine the 3D structure of DDQC supracrystals composed of 70 nm sharp-vertex gold tetrahedra, which were assembled through the slow evaporation of an aqueous solution on hydrophobic polystyrene-coated Si substrates [85]. The 70 nm gold tetrahedra were synthesized using a seed-mediated growth method, purified through a centrifugal force-assisted depletion approach, and post-synthetically functionalized with 11-mercaptoundecanoic acid (MUA). Deprotonated MUA ligands provide a balance between electrostatic repulsion and van der Waals attraction, resulting in hard particle-like interactions. SEM images revealed discrete supracrystals with disk or dome shapes, each spanning several micrometers in diameter. The structural order of individual supracrystals was examined using small-angle X-ray scattering with microfocus X-ray beams. The results showed sharp spots exhibiting 12-fold rotational symmetry, a hallmark of dodecagonal quasicrystals. The 3D structures reconstructed from FIB-SEM tomography closely match the simulation model (Figs. 5(a) and 5(b)). The positions and orientations of the gold nanotetrahedra were revealed through five evenly spaced slices spanning half a z-periodicity. Two pentagonal bipyramids are positioned above and below each 12-tetrahedra ring. The triangular tiles are formed by three 12-tetrahedra rings and a central tetrahedron, which can adopt two orientations (face-up or vertex-up) when viewed along the 12-fold axis. The square tiles consist of four 12-tetrahedra rings enclosing five interstitial tetrahedra, with the outer four arranged to make face-to-face contact with the central tetrahedron. Furthermore, 360° HAADF-STEM tomography was performed on a pillar-shaped cutout prepared by FIB from the central region of a quasicrystalline supracrystal. The reconstructed slices reveal a periodic arrangement of alternating pentagonal bipyramids and 12-tetrahedra rings along the 12-fold axis, consistent with the volume-rendered 3D reconstruction extracted from the FIB-SEM tomogram (Figs. 5(c) and 5(d)). Overall, the surface chemistry of nanotetrahedra and the assembly environment—particularly substrate hydrophobicity—are key parameters for the formation of DDQC supracrystals.

2.4 4D-STEM analysis of nanoparticle assemblies

4D-STEM involves scanning a convergent electron beam over a 2D grid of probe positions, recording a 2D diffraction pattern at each position with a pixelated camera [86]. This process generates a 4D dataset that typically comprises tens of thousands of electron diffraction patterns. Unlike WAED, which provides the ensemble-averaged orientation of nanoparticles in superlattices, 4D-STEM allows for the measurement of the orientation of individual nanoparticles. Orientation mapping requires indexing the Bragg disks within the 4D-STEM dataset. To prevent overlapping of

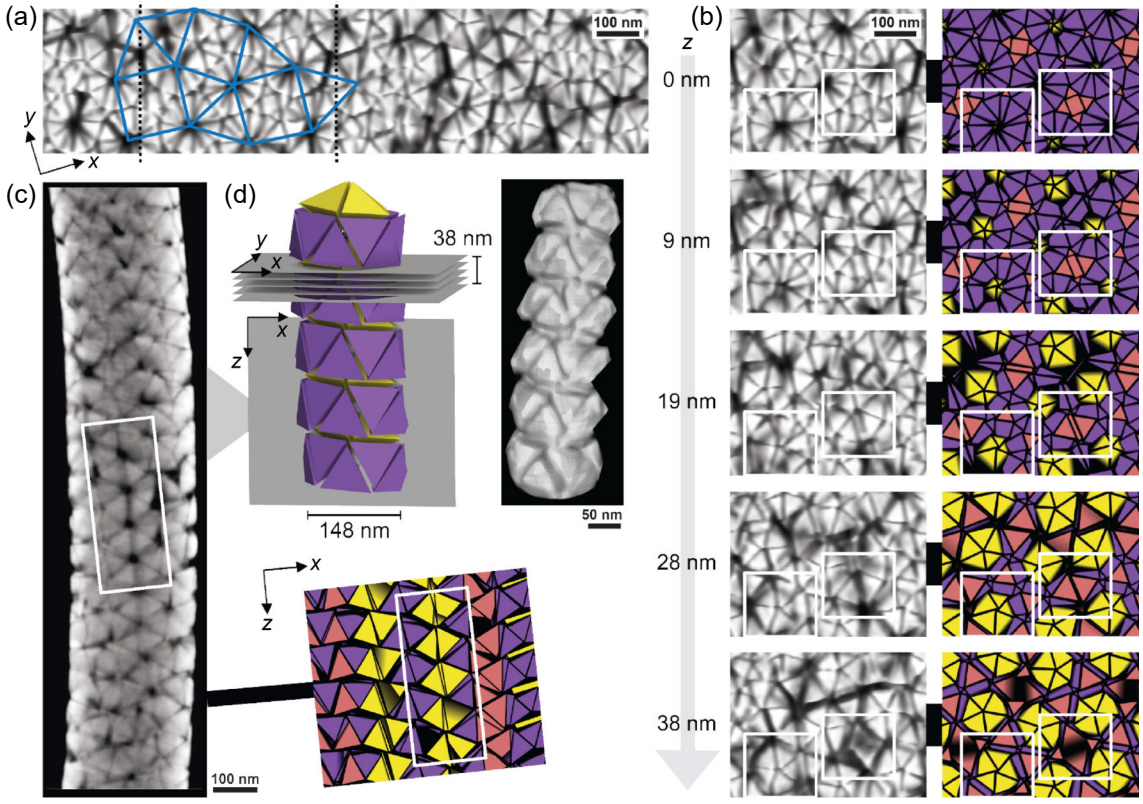

Figure 5 FIB-SEM tomography and electron tomography of dodecagonal quasicrystals self-assembled from sharp-vertex Au tetrahedra with 70-nm edge length. (a) Slice visualization of FIB-SEM tomography reconstruction data and square-triangle tilting analysis. (b) FIB-SEM tomography slices (left) along the 12-fold axis and cuts through the simulation dataset (right) are compared at five different heights. (c) STEM tomography reconstruction of a 250 nm-diameter pillar sample prepared by FIB lift-out from the central region of a quasicrystal. The periodic stacking along the 12-fold axis is confirmed by comparing the STEM tomography slice (left) and a cut through the simulation dataset (right). (d) (left) Schematic depiction of the orientation of cut planes (gray) in (b) and (c) on a log and (right) volume rendering of the FIB-SEM tomography reconstruction. Reproduced with permission from Ref. [85], © American Chemical Society 2023.

adjacent diffraction disks, the convergence angle of the electron probe must be smaller than the Bragg angle of the material being measured. Several open-source packages, such as py4DSTEM [87] and Pyxem [88], have been developed for analyzing 4D-STEM datasets. To generate orientation mapping from a 4D-STEM dataset, a library of diffraction patterns for each possible material orientation is typically precomputed. The orientation is then determined by matching the experimental electron diffraction pattern to the simulated pattern with the highest correlation. Both py4DSTEM and Pyxem are python-based open-source packages that provide orientation mapping workflows in Jupyter notebooks on their public GitHub repositories. While they employ different template matching methods to extract orientations from the 4D-STEM datasets, both packages enable a reliable and fast orientation mapping [87, 88].

4D-STEM has been employed to analyze the orientation distribution of individual nanoparticles within self-assembled superlattices. For example, Cimada daSilva et al. used 4D-STEM to determine the precise position and crystallographic orientation of individual 7 nm PbS nanocrystal in monolayer superlattices at different stages of the transformation from a hexatic to a square-like superlattice [89]. A 2 nm electron probe was used to scan the monolayer superlattice across large fields of view, recording a nanobeam electron diffraction (NBED) pattern at each scan position (Fig. 6). The in-plane and out-of-plane tilt angles were determined by comparing the single-particle NBED patterns of each nanocrystal to a series of simulated patterns. Correlating the orientation of the nanocrystals with the local bond order parameter revealed that the transformation within a grain occurs gradually and is largely driven by the translation of pre-aligned nanocrystals.

3 Electron microscopy characterization of undried nanoparticle assemblies

3.1 Cryogenic transmission electron tomography for 3D structure characterization of nanoparticle assemblies in frozen state

Conventional TEM analyzes dried samples under high vacuum, whereas nanoparticle superlattices formed through non-drying-mediated self-assembly remain stable only in a solvent. Consequently, X-ray scattering techniques are frequently used to analyze these solvent-stabilized assemblies, but they typically yield ensemble-averaged information in reciprocal space. On the other hand, cryogenic TEM (cryo-TEM), originally developed by the structural biology community, is a powerful tool for directly visualizing solvent-stabilized nanoparticle superlattices through solvent vitrification [90–92]. The vitrified TEM sample is prepared by applying a few microliters of aqueous solution onto a glow-discharged holey carbon TEM grid, followed by brief blotting and rapid plunge freezing in liquid ethane. The sample is then cryo-transferred to the microscope for imaging. Cryo-TEM and cryogenic electron tomography (cryo-ET) are conducted at liquid

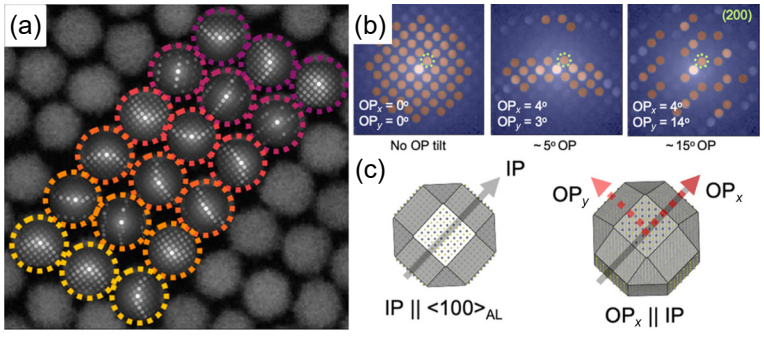

Figure 6 4D-STEM characterization of monolayer superlattices self-assembled from 7 nm PbS truncated cuboctahedron nanocrystals. (a) NBED patterns overlaid with each HAADF-STEM image of the same region. (b) NBED patterns matched to simulated patterns for different out-of-plane and in-plane tilt angles. (c) Illustration of in-plane and out-of-plane angles. Reproduced with permission from Ref. [89], © American Chemical Society 2020.

nitrogen temperatures and under low-dose conditions to maintain the vitrified state of the solvent and prevent thawing.

Cryo-TEM and cryo-ET have been employed to investigate the self-assembly of charged nanoparticles in aqueous solutions [93, 94]. For instance, Kostiainen et al. utilized cryo-ET to characterize the 3D structure of binary nanoparticle superlattices formed by the self-assembly of negatively charged protein cages and positively charged gold nanoparticles in aqueous solution [93]. Due to the inability of the nanoparticle superlattices to withstand drying, cryo-TEM and cryo-ET were conducted on vitrified samples to characterize 2D superlattice projections and 3D structures at the liquid nitrogen temperature. The effective diameters are 28 nm for the negatively charged cowpea chlorotic mottle virus (CCMV), 12 nm for ferritin (FT), and 8.5 nm for the positively charged gold nanoparticles. The interactions between protein cages and gold nanoparticles can be tuned by adjusting the electrolyte concentration and pH to promote BNSL formation. Cryo-ET revealed the formation of a novel fcc AB_8-type BNSL composed of CCMV and gold nanoparticles (Figs. 7(a)–7(d)), as well as a simple cubic CsCl-type BNSL formed by FT and gold nanoparticles. These findings were supported by small-angle X-ray scattering results obtained in aqueous solutions.

Cryo-TEM and cryo-ET can also be used to study less ordered nanoparticle assemblies in solution. For example, Bian et al. used cryo-TEM and cryo-STEM tomography to characterize the structure of aggregates formed immediately after mixing positively charged gold nanoparticles with negatively charged small molecules [29]. Gold nanoparticles with diameters ranging from 2.8 to 13.1 nm were functionalized with (11-mercaptoundecyl)-N,N,N-trimethylammonium (TMA) ligands that feature positively charged ammonium terminal groups. They discovered that small molecules carrying three or more charges could mediate electrostatic attraction between oppositely charged gold nanoparticles, while those with only one or two charges were ineffective. Cryo-TEM and cryo-STEM tomography were employed to characterize the aggregates formed immediately after treatment of the TMA-coated gold nanoparticles with the oligoanion $P_3O_{10}^{5-}$. The tomography reconstruction revealed that the ~ 25 nm aggregates were Mackay icosahedra, with a central nanoparticle surrounded by a 12-nanoparticle icosahedral shell. This inner shell was encased within an outer deltahedral shell composed of 42 nanoparticles, forming a magic number cluster comprising a total of 55 nanoparticles (Figs. 7(e) and 7(f)). The formation of densely packed clusters of like-charged nanoparticles is facilitated by small, oppositely charged molecules that mitigate electrostatic repulsion between the nanoparticles.

3.2 Fast electron tomography for 3D structural characterization of nanoparticle assemblies in liquid environments

The introduction of microfabricated liquid cells has facilitated TEM characterization of samples within liquid environments. These cells consist of two electron-transparent windows, typically less than 50 nm thick, that enclose the liquid and isolate it from the microscope's vacuum. Electron tomography of nanoparticle assemblies in liquid can provide accurate 3D representations of their native solvated state, closely resembling the results achieved with cryo-TEM tomography. However, several challenges remain, including the limited tilt range imposed by the liquid cell's geometry, background noise from the liquid and silicon nitride windows, and a weak signal-to-noise ratio due to the need for low-dose imaging to prevent radiolysis. The restricted tilt range results in a missing wedge artifact, which compromises the quality of the tomographic reconstruction. Overcoming these challenges requires improvements in liquid cell design and the development of innovative methods for tilt series acquisition, alignment, and reconstruction. For instance, unlike conventional electron tomography, which typically requires tens of minutes to acquire a tilt series, fast electron tomography reduces acquisition time to just a few minutes or even less than one minute by continuously tilting the sample while capturing 2D projection images [95–97].

Recently, Arenas Esteban et al. demonstrated the utility of fast electron tomography for 3D structural characterization of nanoparticle assemblies in liquid cells [98]. Two types of liquid cells were used: one with a 90° tilt range and a 500 nm window gap, and another with a 140° tilt range and a 100 nm window gap. Approximately 2 μL of nanoparticle solution was introduced into the liquid cell, assisted by capillary forces. The liquid cell, sealed with water-resistant glue, was mounted onto a single-tilt holder for fast tomography acquisition. They developed an optimized workflow for the acquisition, alignment, and reconstruction of nanoparticle assemblies in liquid environments. This included an advanced reconstruction method that combined compressed sensing with the discrete algebraic reconstruction technique, significantly improving the accuracy of tomography reconstructions. Fast electron tomography of cetyltrimethylammonium bromide (CTAB)-stabilized gold nanorods showed that surface-to-surface distances were shorter in vacuum (2–4 nm) compared to those in liquid (6–8 nm), as illustrated in Fig. 8. These findings underscore the importance of liquid cell electron tomography for accurately capturing the 3D structures of nanoparticle assemblies in their native liquid environments.

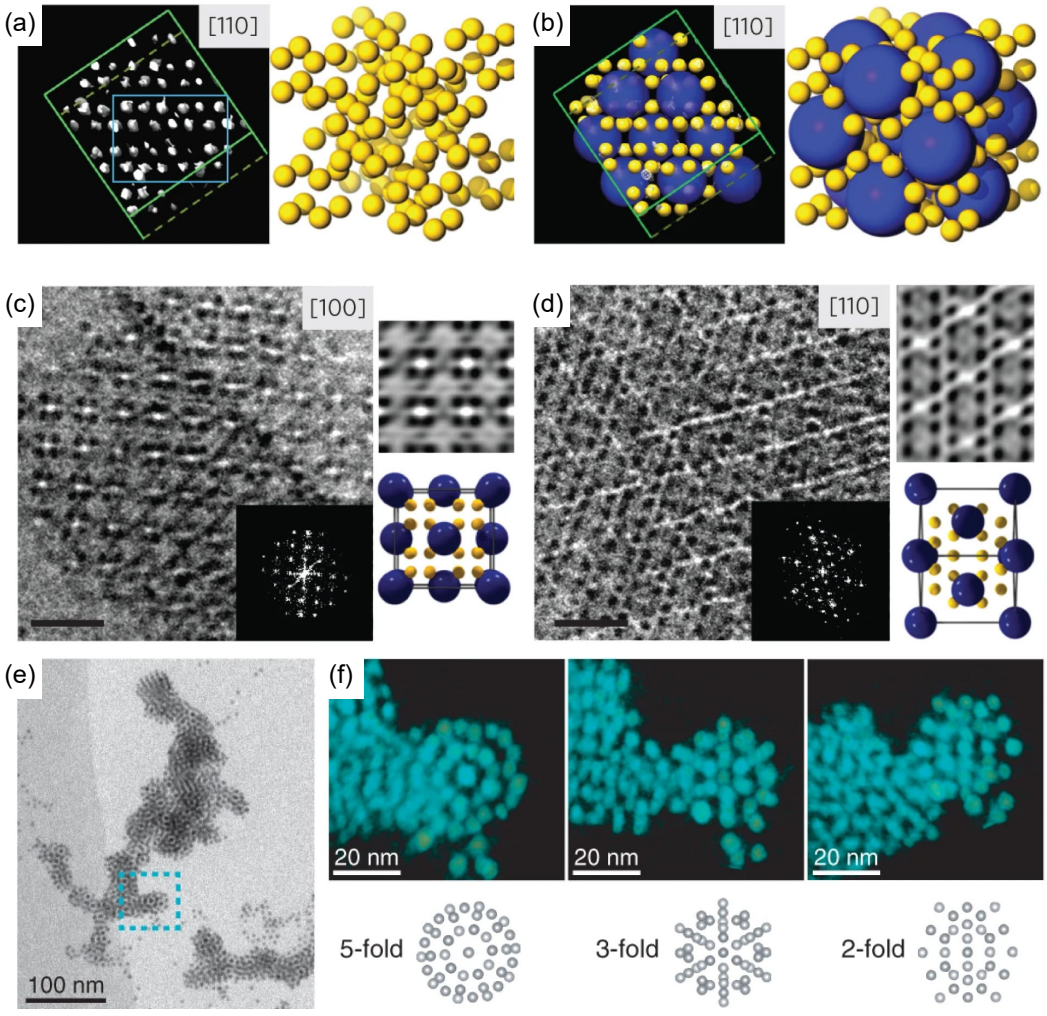

Figure 7 Cryo-TEM and cryo-ET of nanoparticle superlattices. Cryo-ET reconstruction data (a), structural model (b), cryo-TEM images of [100] and [110] projections ((c) and (d)) of vitrified AB_8-type superlattices self-assembled from negatively charged CCMV cages and positively charged 2.6 nm Au nanoparticles. Scale bars: 50 nm. Reproduced with permission from Ref. [93], © Macmillan Publishers Limited 2013. (e) Cryo-STEM bright-field image of a vitrified Au·TMA/$P_3O_{10}^{5-}$ aggregate. (f) (top) Voxel projections of the cryo-tomography reconstruction of the Mackay cluster marked in (e) and (bottom) corresponding 2D projections of structural models. Reproduced with permission from Ref. [29], © Bian, T. et al. 2021.

4 LCTEM for direct imaging of nanoparticle self-assembly dynamics

Due to advancements in microfabricated liquid cells and specialized sample holders, LCTEM has emerged as a powerful technique for studying the dynamics of nanoparticle self-assembly in liquid environments [90, 99–115]. While X-ray scattering techniques have been widely employed to investigate nanoparticle self-assembly in solutions, they are limited to providing ensemble-level information in reciprocal space. In contrast, LCTEM enables direct imaging of dynamic processes at the single-particle level in real space. Nanometer-scale image resolution is achieved using microfabricated liquid cells with thin silicon nitride or graphene windows and spacers that isolate the liquid from the vacuum environment within the TEM. The holder's flow capability allows for the introduction and exchange of solutions within the liquid cells before or during imaging. Additionally, electrodes patterned on the silicon nitride chips and sample holder enable the application of electric fields and temperature jumps as stimuli for studying dynamic processes. The electron beam plays an important role in studying nanoparticle self-assembly with LCTEM. It functions not only as an imaging source but can also affect the liquid environment within the cells by inducing solution radiolysis and charging the silicon nitride windows and nanoparticles. The large, time-resolved TEM datasets with low signal-to-noise ratios present significant challenges for efficient data processing and analysis. These challenges can be overcame by leveraging machine learning and deep learning techniques [116–121].

Ou et al. used LCTEM to directly observe a two-step nonclassical nucleation pathway in nanoparticle assembly [107], capturing the transition of dispersed triangular gold nanoprisms into a superlattice in aqueous solution (Fig. 9(a)). Before electron beam illumination, triangular gold nanoprisms with a side length of 100.5 nm and a thickness of 7.5 nm were dispersed in the solution due to electrostatic repulsion imparted by the negatively charged thiolated ligands. The electron beam rapidly increases ionic strength in the illuminated region through water radiolysis, reducing electrostatic repulsion and causing the gold nanoprisms to stack into vertically aligned columns on the SiN_x chip. The gold nanoprisms within each column exhibited random horizontal alignment, creating columns that formed a hexagonal lattice appearing as circular discs under TEM. The evolution of liquid and

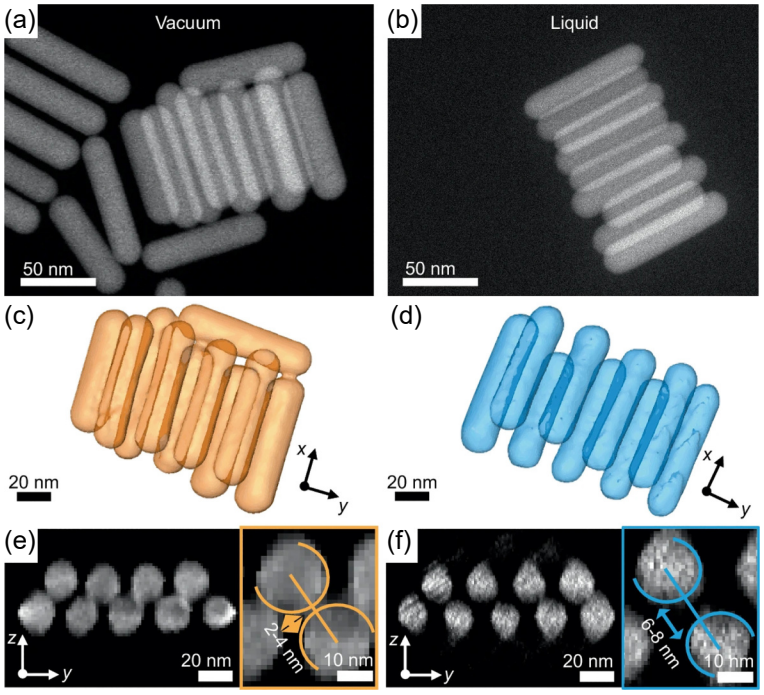

Figure 8 Fast electron tomography of Au nanorod bilayer assemblies in vacuum and liquid solution. 2D HAADF-STEM images ((a) and (b)), 3D STEM-tomography reconstructions ((c) and (d)) and orthogonal slice views of superlattices self-assembled from two layers of Au nanorods in vacuum ((a), (c), and (e)) and liquid solution ((b), (d), and (f)), respectively. Reproduced with permission from Ref. [98], © Arenas Esteban, D. et al. 2024.

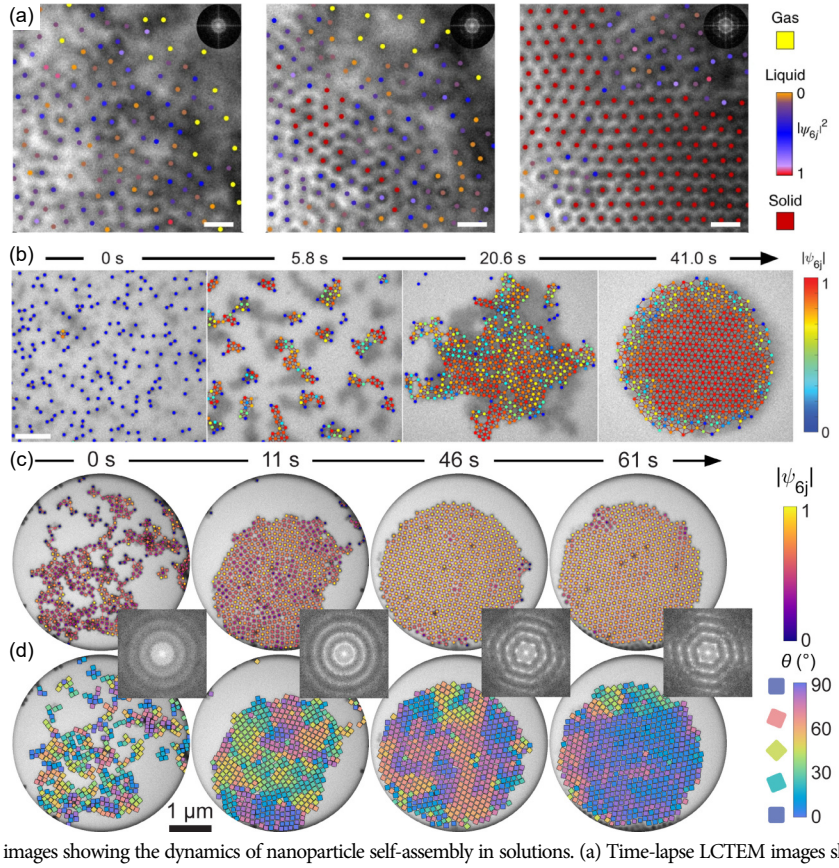

Figure 9 Time-lapse LCTEM images showing the dynamics of nanoparticle self-assembly in solutions. (a) Time-lapse LCTEM images show the self-assembly process of gold triangular nanoprisms in aqueous solution, with nanoprism columns colored according to $|\psi_{6j}|^2$. Reproduced with permission from Ref. [107], © Ou, Z. H. et al. 2019. (b) Time-lapse LCTEM images show the self-assembly process of gold nanospheres in nonaqueous solution, with nanoparticle centroids color-coded according to $|\psi_{6j}|$. Reproduced with permission from Ref. [112], © American Chemical Society 2022. Time-lapse LCTEM images show the self-assembly process of gold nanocubes in nonaqueous solution, with nanocube centroids colored according to $|\psi_{6j}|$ (c), and nanocubes colored according to their orientations (d). Reproduced with permission from Ref. [114], © Zhong, Y. X. et al. 2024.

solid column populations followed a two-step nonclassical crystallization pathway which involved a dense, amorphous intermediate.

Using LCTEM, Zhong et al. revealed a multistep crystallization pathway for nanoparticle self-assembly in a mixed octane-butanol solvent [112], capturing the entire process from dispersed nanoparticles to ordered superlattices with single-particle resolution (Fig. 9(b)). Prior to TEM imaging, 68.1 nm gold nanospheres grafted with 3.2 kDa thiol-terminated polystyrene were deposited onto the Si_3N_4 windows. However, within seconds of electron beam illumination, they began to move due to electron-beam-induced positive charging of the Si_3N_4 windows and the gold nanospheres. A multistep crystallization pathway comprising four distinct stages—gas state, cluster state, polycrystalline state, and single crystalline solid state—was unveiled using deep learning-assisted image segmentation and order parameter analysis. The solvent composition was identified as the key parameter for tuning interparticle interactions and the assembly behavior of polystyrene-grafted Au nanospheres. LCTEM also revealed the formation, migration, and annihilation of structural defects in nanoparticle superlattices, such as vacancies, dislocations, and grain boundaries.

Recently, Zhong et al. reported LCTEM imaging of the self-assembly pathways of gold nanocubes into various superlattice structures [114], with the assembly process governed by solvent composition (Figs. 9(c) and 9(d)). Theoretical analysis and molecular dynamics simulations suggest that the interplay between van der Waals attraction and electrostatic repulsion in different solvents controls superlattice formation. As the solvent polarity decreased with an increasing ratio of octane to butanol, the formation of square-like (SQ), rhombic (RB), and hexagonal rotator (HR) phases of 2D superlattices composed of 87.4 nm gold nanocubes was observed. Distinct self-assembly pathways for the three phases were identified through deep learning-assisted image segmentation and analyzed using various order parameters. The evolution of lattice translational order and particle orientational order was largely decoupled during the assembly of the HR phase, while strong coupling was observed for the SQ phase. In contrast, the degree of coupling varied at different stages of the assembly process for the RB phase. They also demonstrated real-time control of solid–solid transitions via *in situ* rapid solvent exchange. LCTEM revealed two pathways for the RB-to-SQ transition: one involving an HR-like intermediate and the other characterized by lattice distortion resulting from the collective rotation of gold nanocubes, influenced by their local densities.

5 Outlook and perspective

In this review, we discussed the utility and advantages of various electron microscopy techniques for characterizing the structures and formation pathways of nanoparticle assemblies, spanning from conventional imaging and diffraction to advanced techniques such as electron tomography, FIB-SEM tomography, cryogenic electron tomography, fast electron tomography, 4D-STEM, and LCTEM (Table 1). These methods facilitate the acquisition of 2D and 3D structural information of nanoparticle superlattices in dry, frozen, and liquid states. We also highlighted the advantages of LCTEM for studying dynamic processes of nanoparticle assembly in liquid environments. Furthermore, we discussed the development of advanced data processing and analysis algorithms and their integration into open-source software for tomography reconstruction and 4D-STEM data analysis. The incorporation of artificial intelligence and machine learning techniques has been instrumental in managing large and complex datasets, including those with low signal-to-noise ratios, with many open-source Python codes available to researchers. We anticipate that the extensive electron microscopy toolkit, combined with advanced computational algorithms and machine learning, will continue to offer new insights and deepen our understanding in future research on nanoparticle self-assembly.

Data availability

All data needed to support the conclusions in the paper are presented in the manuscript. Additional data related to this paper may be requested from the corresponding author upon request.

Acknowledgements

We acknowledge the support from the US National Science Foundation under awards DMR-2102526 and CBET-2223453.

Declaration of competing interest

All the contributing authors report no conflict of interests in this work.

Author contribution statement

J. C.: Writing manuscript. C. Y. Y.: Writing manuscript. B. X. Z.: Writing manuscript. C. L. H.: Writing manuscript. F. R. C.: Writing manuscript. H. Y. D.: Writing manuscript. X. C. Y.: Project

Table 1 Summary of advantages and disadvantages of various electron microscopy techniques in nanoparticle self-assembly research

Technique	Advantage	Disadvantage
TEM imaging	Fast, accessible in every TEM	Only provide 2D projections
SAED/WAED	Fast, accessible in every TEM	Only provide 2D projections
SEM imaging	Fast, accessible in every SEM	Only provide surface information
TEM/STEM tomography	Enable 3D information in dry state	Require high tilting holder
FIB-SEM tomography	Enable 3D information in dry state	Require FIB-SEM dual probe workstation
4D-STEM	Provide orientation mapping	Require 4D-STEM acquisition capability
Cryo-TEM/cryo-STEM tomography	Provide 3D information in frozen hydrated state	Require cryo-TEM holder or cryo-TEM
Fast electron tomography	Provide 3D information in liquid environment	Require liquid cells and specific data acquisition and reconstruction algorithms
LCTEM	Provide the dynamics in liquid environment	Require liquid cells and specific TEM holders

administration, funding acquisition, writing manuscript. All the authors have approved the final manuscript.

Use of AI statement

None.

References

[1] Boles, M. A.; Engel, M.; Talapin, D. V. Self-assembly of colloidal nanocrystals: From intricate structures to functional materials. *Chem. Rev.* **2016**, *116*, 11220–11289.

[2] Bassani, C. L.; van Anders, G.; Banin, U.; Baranov, D.; Chen, Q.; Dijkstra, M.; Dimitriyev, M. S.; Efrati, E.; Faraudo, J.; Gang, O. et al. Nanocrystal assemblies: Current advances and open problems. *ACS Nano* **2024**, *18*, 14791–14840.

[3] Urban, J. J.; Talapin, D. V.; Shevchenko, E. V.; Kagan, C. R.; Murray, C. B. Synergism in binary nanocrystal superlattices leads to enhanced p-type conductivity in self-assembled PbTe/Ag_2Te thin films. *Nat. Mater.* **2007**, *6*, 115–121.

[4] Mueggenburg, K. E.; Lin, X. M.; Goldsmith, R. H.; Jaeger, H. M. Elastic membranes of close-packed nanoparticle arrays. *Nat. Mater.* **2007**, *6*, 656–660.

[5] Chen, J.; Dong, A. G.; Cai, J.; Ye, X. C.; Kang, Y. J.; Kikkawa, J. M.; Murray, C. B. Collective dipolar interactions in self-assembled magnetic binary nanocrystal superlattice membranes. *Nano Lett.* **2010**, *10*, 5103–5108.

[6] Dong, A. G.; Chen, J.; Vora, P. M.; Kikkawa, J. M.; Murray, C. B. Binary nanocrystal superlattice membranes self-assembled at the liquid-air interface. *Nature* **2010**, *466*, 474–477.

[7] Chen, J.; Ye, X. C.; Oh, S. J.; Kikkawa, J. M.; Kagan, C. R.; Murray, C. B. Bistable magnetoresistance switching in exchange-coupled $CoFe_2O_4$-Fe_3O_4 binary nanocrystal superlattices by self-assembly and thermal annealing. *ACS Nano* **2013**, *7*, 1478–1486.

[8] Kang, Y. J.; Ye, X. C.; Chen, J.; Cai, Y.; Diaz, R. E.; Adzic, R. R.; Stach, E. A.; Murray, C. B. Design of Pt-Pd binary superlattices exploiting shape effects and synergistic effects for oxygen reduction reactions. *J. Am. Chem. Soc.* **2013**, *135*, 42–45.

[9] Ye, X. C.; Chen, J.; Diroll, B. T.; Murray, C. B. Tunable plasmonic coupling in self-assembled binary nanocrystal superlattices studied by correlated optical microspectrophotometry and electron microscopy. *Nano Lett.* **2013**, *13*, 1291–1297.

[10] Murray, C. B.; Norris, D. J.; Bawendi, M. G. Synthesis and characterization of nearly monodisperse CdE (E = sulfur, selenium, tellurium) semiconductor nanocrystallites. *J. Am. Chem. Soc.* **1993**, *115*, 8706–8715.

[11] Xia, Y. N.; Xiong, Y. J.; Lim, B.; Skrabalak, S. E. Shape-controlled synthesis of metal nanocrystals: Simple chemistry meets complex physics. *Angew. Chem., Int. Ed.* **2008**, *48*, 60–103.

[12] Ye, X. C.; Collins, J. E.; Kang, Y. J.; Chen, J.; Chen, D. T.; Yodh, A. G.; Murray, C. B. Morphologically controlled synthesis of colloidal upconversion nanophosphors and their shape-directed self-assembly. *Proc. Natl. Acad. Sci. USA* **2010**, *107*, 22430–22435.

[13] Ye, X. C.; Zheng, C.; Chen, J.; Gao, Y. Z.; Murray, C. B. Using binary surfactant mixtures to simultaneously improve the dimensional tunability and monodispersity in the seeded growth of gold nanorods. *Nano Lett.* **2013**, *13*, 765–771.

[14] O'Brien, M. N.; Jones, M. R.; Brown, K. A.; Mirkin, C. A. Universal noble metal nanoparticle seeds realized through iterative reductive growth and oxidative dissolution reactions. *J. Am. Chem. Soc.* **2014**, *136*, 7603–7606.

[15] Liu, Z. K.; Zhong, Y. X.; Shafei, I.; Borman, R.; Jeong, S.; Chen, J.; Losovyj, Y.; Gao, X. F.; Li, N.; Du, Y. P. et al. Tuning infrared plasmon resonances in doped metal-oxide nanocrystals through cation-exchange reactions. *Nat. Commun.* **2019**, *10*, 1394.

[16] Jeong, S.; Liu, Y.; Zhong, Y. X.; Zhan, X.; Li, Y. D.; Wang, Y.; Cha, P. M.; Chen, J.; Ye, X. C. Heterometallic seed-mediated growth of monodisperse colloidal copper nanorods with widely tunable plasmonic resonances. *Nano Lett.* **2020**, *20*, 7263–7271.

[17] Liu, Y.; Li, Y. D.; Jeong, S.; Wang, Y.; Chen, J.; Ye, X. C. Colloidal synthesis of nanohelices via bilayer lattice misfit. *J. Am. Chem. Soc.* **2020**, *142*, 12777–12783.

[18] Murray, C. B.; Kagan, C. R.; Bawendi, M. G. Self-organization of CdSe nanocrystallites into three-dimensional quantum dot superlattices. *Science* **1995**, *270*, 1335–1338.

[19] Shevchenko, E. V.; Talapin, D. V.; Kotov, N. A.; O'Brien, S.; Murray, C. B. Structural diversity in binary nanoparticle superlattices. *Nature* **2006**, *439*, 55–59.

[20] Ye, X. C.; Zhu, C. H.; Ercius, P.; Raja, S. N.; He, B.; Jones, M. R.; Hauwiller, M. R.; Liu, Y.; Xu, T.; Alivisatos, A. P. Structural diversity in binary superlattices self-assembled from polymer-grafted nanocrystals. *Nat. Commun.* **2015**, *6*, 10052.

[21] Yun, H.; Lee, Y. J.; Xu, M.; Lee, D. C.; Stein, G. E.; Kim, B. J. Softness- and size-dependent packing symmetries of polymer-grafted nanoparticles. *ACS Nano* **2020**, *14*, 9644–9651.

[22] Liu, Y.; Klement, M.; Wang, Y.; Zhong, Y. X.; Zhu, B. X.; Chen, J.; Engel, M.; Ye, X. C. Macromolecular ligand engineering for programmable nanoprism assembly. *J. Am. Chem. Soc.* **2021**, *143*, 16163–16172.

[23] Jishkariani, D.; Diroll, B. T.; Cargnello, M.; Klein, D. R.; Hough, L. A.; Murray, C. B.; Donnio, B. Dendron-mediated engineering of interparticle separation and self-assembly in dendronized gold nanoparticles superlattices. *J. Am. Chem. Soc.* **2015**, *137*, 10728–10734.

[24] Elbert, K. C.; Vo, T.; Krook, N. M.; Zygmunt, W.; Park, J.; Yager, K. G.; Composto, R. J.; Glotzer, S. C.; Murray, C. B. Dendrimer ligand directed nanoplate assembly. *ACS Nano* **2019**, *13*, 14241–14251.

[25] Nykypanchuk, D.; Maye, M. M.; van der Lelie, D.; Gang, O. DNA-guided crystallization of colloidal nanoparticles. *Nature* **2008**, *451*, 549–552.

[26] Park, S. Y.; Lytton-Jean, A. K. R.; Lee, B.; Weigand, S.; Schatz, G. C.; Mirkin, C. A. DNA-programmable nanoparticle crystallization. *Nature* **2008**, *451*, 553–556.

[27] Zhou, W. J.; Lim, Y.; Lin, H. X.; Lee, S.; Li, Y. W.; Huang, Z. Y.; Du, J. S.; Lee, B.; Wang, S. Z.; Sánchez-Iglesias, A. et al. Colloidal quasicrystals engineered with DNA. *Nat. Mater.* **2024**, *23*, 424–428.

[28] Kalsin, A. M.; Fialkowski, M.; Paszewski, M.; Smoukov, S. K.; Bishop, K. J. M.; Grzybowski, B. A. Electrostatic self-assembly of binary nanoparticle crystals with a diamond-like lattice. *Science* **2006**, *312*, 420–424.

[29] Bian, T.; Gardin, A.; Gemen, J.; Houben, L.; Perego, C.; Lee, B.; Elad, N.; Chu, Z. L.; Pavan, G. M.; Klajn, R. Electrostatic co-assembly of nanoparticles with oppositely charged small molecules into static and dynamic superstructures. *Nat. Chem.* **2021**, *13*, 940–949.

[30] Coropceanu, I.; Janke, E. M.; Portner, J.; Haubold, D.; Nguyen, T. D.; Das, A.; Tanner, C. P. N.; Utterback, J. K.; Teitelbaum, S. W.; Hudson, M. H. et al. Self-assembly of nanocrystals into strongly electronically coupled all-inorganic supercrystals. *Science* **2022**, *375*, 1422–1426.

[31] Zhang, J. Y.; Santos, P. J.; Gabrys, P. A.; Lee, S.; Liu, C.; Macfarlane, R. J. Self-assembling nanocomposite tectons. *J. Am. Chem. Soc.* **2016**, *138*, 16228–16231.

[32] Yi, C. L.; Liu, H.; Zhang, S. Y.; Yang, Y. Q.; Zhang, Y.; Lu, Z. Y.; Kumacheva, E.; Nie, Z. H. Self-limiting directional nanoparticle bonding governed by reaction stoichiometry. *Science* **2020**, *369*, 1369–1374.

[33] Duan, H. Y.; Jia, Z. Y.; Liaqat, M.; Mellor, M. D.; Tan, H. Y.; Nieh, M. P.; Lin, Y.; Link, S.; Landes, C. F.; He, J. Site-specific chemistry on gold nanorods: Curvature-guided surface dewetting and supracolloidal polymerization. *ACS Nano* **2023**, *17*, 12788–12797.

[34] Ning, Y. F.; Yang, S. S.; Yang, D. B.; Cai, Y. Y.; Xu, J.; Li, R. P.; Zhang, Y. G.; Kagan, C. R.; Saven, J. G.; Murray, C. B. Dynamic nanocrystal superlattices with thermally triggerable lubricating ligands. *J. Am. Chem. Soc.* **2024**, *146*, 3785–3795.

[35] Yang, S. S.; Ning, Y. F.; Zhang, Y. G.; Murray, C. B. Growth of nanocrystal superlattices from liquid crystals. *J. Am. Chem. Soc.* **2024**, *146*, 11043–11047.

[36] Talapin, D. V.; Shevchenko, E. V.; Kornowski, A.; Gaponik, N.; Haase, M.; Rogach, A. L.; Weller, H. A new approach to crystallization of CdSe nanoparticles into ordered three-dimensional superlattices. *Adv. Mater.* **2001**, *13*, 1868–1871.

[37] Williams, D. B.; Carter, C. B. *Transmission Electron Microscopy: A Textbook for Materials Science*; Springer: New York, 2009.

[38] Carter, C. B.; Williams, D. B. *Transmission Electron Microscopy: Diffraction, Imaging, and Spectrometry*; Springer: Cham, 2016.

[39] Zuo, J. M.; Spence, J. C. H. *Advanced Transmission Electron Microscopy*; Springer: New York, 2017.

[40] Talapin, D. V.; Shevchenko, E. V.; Bodnarchuk, M. I.; Ye, X. C.; Chen, J.; Murray, C. B. Quasicrystalline order in self-assembled binary nanoparticle superlattices. *Nature* **2009**, *461*, 964–967.

[41] Dong, A. G.; Ye, X. C.; Chen, J.; Murray, C. B. Two-dimensional binary and ternary nanocrystal superlattices: The case of monolayers and bilayers. *Nano Lett.* **2011**, *11*, 1804–1809.

[42] Henzie, J.; Grünwald, M.; Widmer-Cooper, A.; Geissler, P. L.; Yang, P. D. Self-assembly of uniform polyhedral silver nanocrystals into densest packings and exotic superlattices. *Nat. Mater.* **2012**, *11*, 131–137.

[43] Wang, T.; Zhuang, J. Q.; Lynch, J.; Chen, O.; Wang, Z. L.; Wang, X. R.; LaMontagne, D. ;Wu, H. M.; Wang, Z. W.; Cao, Y. C. Self-assembled colloidal superparticles from nanorods. *Science* **2012**, *338*, 358–363.

[44] Ye, X. C.; Chen, J.; Engel, M.; Millan, J. A.; Li, W. B.; Qi, L. B.; Xing, G. Z.; Collins, J. E.; Kagan, C. R.; Li, J. et al. Competition of shape and interaction patchiness for self-assembling nanoplates. *Nat. Chem.* **2013**, *5*, 466–473.

[45] Ye, X. C.; Millan, J. A.; Engel, M.; Chen, J.; Diroll, B. T.; Glotzer, S. C.; Murray, C. B. Shape alloys of nanorods and nanospheres from self-assembly. *Nano Lett.* **2013**, *13*, 4980–4988.

[46] Paik, T.; Murray, C. B. Shape-directed binary assembly of anisotropic nanoplates: A nanocrystal puzzle with shape-complementary building blocks. *Nano Lett.* **2013**, *13*, 2952–2956.

[47] Singh, G.; Chan, H.; Baskin, A.; Gelman, E.; Repnin, N.; Král, P.; Klajn, R. Self-assembly of magnetite nanocubes into helical superstructures. *Science* **2014**, *345*, 1149–1153.

[48] Paik, T.; Diroll, B. T.; Kagan, C. R.; Murray, C. B. Binary and ternary superlattices self-assembled from colloidal nanodisks and nanorods. *J. Am. Chem. Soc.* **2015**, *137*, 6662–6669.

[49] Chen, J.; Fasoli, A.; Cushen, J. D.; Wan, L.; Ruiz, R. Self-assembly and directed assembly of polymer grafted nanocrystals via solvent annealing. *Macromolecules* **2017**, *50*, 9636–9646.

[50] Yang, Y. C.; Wang, B. W.; Shen, X. D.; Yao, L. Y.; Wang, L.; Chen, X.; Xie, S. H.; Li, T. T.; Hu, J. H.; Yang, D. et al. Scalable assembly of crystalline binary nanocrystal superparticles and their enhanced magnetic and electrochemical properties. *J. Am. Chem. Soc.* **2018**, *140*, 15038–15047.

[51] Yun, H.; Yu, J. W.; Lee, Y. J.; Kim, J. S.; Park, C. H.; Nam, C.; Han, J.; Heo, T. Y.; Choi, S. H.; Lee, D. C. et al. Symmetry transitions of polymer-grafted nanoparticles: Grafting density effect. *Chem. Mater.* **2019**, *31*, 5264–5273.

[52] Wang, Y.; Chen, J.; Zhu, C. H.; Zhu, B. X.; Jeong, S.; Yi, Y.; Liu, Y.; Fiadorwu, J.; He, P.; Ye, X. C. Kinetically controlled self-assembly of binary polymer-grafted nanocrystals into ordered superstructures via solvent vapor annealing. *Nano Lett.* **2021**, *21*, 5053–5059.

[53] Wang, Y.; Chen, J.; Zhong, Y. X.; Jeong, S.; Li, R. P.; Ye, X. C. Structural diversity in dimension-controlled assemblies of tetrahedral gold nanocrystals. *J. Am. Chem. Soc.* **2022**, *144*, 13538–13546.

[54] Ye, X. C.; Chen, J.; Eric Irrgang, M.; Engel, M.; Dong, A. G.; Glotzer, S. C.; Murray, C. B. Quasicrystalline nanocrystal superlattice with partial matching rules. *Nat. Mater.* **2017**, *16*, 214–219.

[55] Chen, J.; Ye, X. C.; Murray, C. B. Systematic electron crystallographic studies of self-assembled binary nanocrystal superlattices. *ACS Nano* **2010**, *4*, 2374–2381.

[56] Ye, X. C.; Chen, J.; Murray, C. B. Polymorphism in self-assembled AB_6 binary nanocrystal superlattices. *J. Am. Chem. Soc.* **2011**, *133*, 2613–2620.

[57] Bodnarchuk, M. I.; Kovalenko, M. V.; Heiss, W.; Talapin, D. V. Energetic and entropic contributions to self-assembly of binary nanocrystal superlattices: Temperature as the structure-directing factor. *J. Am. Chem. Soc.* **2010**, *132*, 11967–11977.

[58] Boles, M. A.; Talapin, D. V. Self-assembly of tetrahedral CdSe nanocrystals: Effective "patchiness" via anisotropic steric interaction. *J. Am. Chem. Soc.* **2014**, *136*, 5868–5871.

[59] Nagaoka, Y.; Tan, R.; Li, R. P.; Zhu, H.; Eggert, D.; Wu, Y. A.; Liu, Y. Z.; Wang, Z. W.; Chen, O. Superstructures generated from truncated tetrahedral quantum dots. *Nature* **2018**, *561*, 378–382.

[60] Evers, W. H.; Friedrich, H.; Filion, L.; Dijkstra, M.; Vanmaekelbergh, D. Observation of a ternary nanocrystal superlattice and its structural characterization by electron tomography. *Angew. Chem., Int. Ed.* **2009**, *48*, 9655–9657.

[61] Friedrich, H.; Gommes, C. J.; Overgaag, K.; Meeldijk, J. D.; Evers, W. H.; de Nijs, B.; Boneschanscher, M. P.; de Jongh, P. E.; Verkleij, A. J.; de Jong, K. P. et al. Quantitative structural analysis of binary nanocrystal superlattices by electron tomography. *Nano Lett.* **2009**, *9*, 2719–2724.

[62] Miszta, K.; de Graaf, J.; Bertoni, G.; Dorfs, D.; Brescia, R.; Marras, S.; Ceseracciu, L.; Cingolani, R.; van Roij, R.; Dijkstra, M. et al. Hierarchical self-assembly of suspended branched colloidal nanocrystals into superlattice structures. *Nat. Mater.* **2011**, *10*, 872–876.

[63] Zhang, J.; Luo, Z. P.; Quan, Z. W.; Wang, Y. X.; Kumbhar, A.; Smilgies, D. M.; Fang, J. Y. Low packing density self-assembled superstructure of octahedral Pt_3Ni nanocrystals. *Nano Lett.* **2011**, *11*, 2912–2918.

[64] Florea, I.; Demortière, A.; Petit, C.; Bulou, H.; Hirlimann, C.; Ersen, O. 3D quantitative analysis of platinum nanocrystal superlattices by electron tomography. *ACS Nano* **2012**, *6*, 2574–2581.

[65] Zhang, J.; Luo, Z. P.; Martens, B.; Quan, Z. W.; Kumbhar, A.; Porter, N.; Wang, Y. X.; Smilgies, D. M.; Fang, J. Y. Reversible Kirkwood–Alder transition observed in Pt_3Cu_2 nanoctahedron assemblies under controlled solvent annealing/drying conditions. *J. Am. Chem. Soc.* **2012**, *134*, 14043–14049.

[66] Boneschanscher, M. P.; Evers, W. H.; Qi, W. K.; Meeldijk, J. D.; Dijkstra, M.; Vanmaekelbergh, D. Electron tomography resolves a novel crystal structure in a binary nanocrystal superlattice. *Nano Lett.* **2013**, *13*, 1312–1316.

[67] Jishkariani, D.; Wu, Y. T.; Wang, D.; Liu, Y.; van Blaaderen, A.; Murray, C. B. Preparation and self-assembly of dendronized janus Fe_3O_4-Pt and Fe_3O_4-Au heterodimers. *ACS Nano* **2017**, *11*, 7958–7966.

[68] Udayabhaskararao, T.; Altantzis, T.; Houben, L.; Coronado-Puchau, M.; Langer, J.; Popovitz-Biro, R.; Liz-Marzán, L. M.; Vuković, L.; Král, P.; Bals, S. et al. Tunable porous nanoallotropes prepared by post-assembly etching of binary nanoparticle superlattices. *Science* **2017**, *358*, 514–518.

[69] Nagaoka, Y.; Zhu, H.; Eggert, D.; Chen, O. Single-component

quasicrystalline nanocrystal superlattices through flexible polygon tiling rule. *Science* **2018**, *362*, 1396–1400.

[70] van der Burgt, J. S.; Geuchies, J. J.; van der Meer, B.; Vanrompay, H.; Zanaga, D.; Zhang, Y.; Albrecht, W.; Petukhov, A. V.; Filion, L.; Bals, S. et al. Cuboidal supraparticles self-assembled from cubic $CsPbBr_3$ perovskite nanocrystals. *J. Phys. Chem. C* **2018**, *122*, 15706–15712.

[71] Cherniukh, I.; Rainò, G.; Stöferle, T.; Burian, M.; Travesset, A.; Naumenko, D.; Amenitsch, H.; Erni, R.; Mahrt, R. F.; Bodnarchuk, M. I. et al. Perovskite-type superlattices from lead halide perovskite nanocubes. *Nature* **2021**, *593*, 535–542.

[72] Qian, Y. W.; da Silva, A.; Yu, E.; Anderson, C. L.; Liu, Y.; Theis, W.; Ercius, P.; Xu, T. Crystallization of nanoparticles induced by precipitation of trace polymeric additives. *Nat. Commun.* **2021**, *12*, 2767.

[73] Frank, J. *Electron Tomography: Methods for Three-Dimensional Visualization of Structures in the Cell*; Springer: New York, 2006.

[74] Mastronarde, D. N. Dual-axis tomography: An approach with alignment methods that preserve resolution. *J. Struct. Biol.* **1997**, *120*, 343–352.

[75] Mastronarde, D. N.; Held, S. R. Automated tilt series alignment and tomographic reconstruction in IMOD. *J. Struct. Biol.* **2017**, *197*, 102–113.

[76] van Aarle, W.; Palenstijn, W. J.; De Beenhouwer, J.; Altantzis, T.; Bals, S.; Batenburg, K. J.; Sijbers, J. The ASTRA Toolbox: A platform for advanced algorithm development in electron tomography. *Ultramicroscopy* **2015**, *157*, 35–47.

[77] Schwartz, J.; Harris, C.; Pietryga, J.; Zheng, H. H.; Kumar, P.; Visheratina, A.; Kotov, N. A.; Major, B.; Avery, P.; Ercius, P. et al. Real-time 3D analysis during electron tomography using tomviz. *Nat. Commun.* **2022**, *13*, 4458.

[78] Gilbert, P. Iterative methods for the three-dimensional reconstruction of an object from projections. *J. Theor. Biol.* **1972**, *36*, 105–117.

[79] Wang, D.; Dasgupta, T.; van der Wee, E. B.; Zanaga, D.; Altantzis, T.; Wu, Y. T.; Coli, G. M.; Murray, C. B.; Bals, S.; Dijkstra, M. et al. Binary icosahedral clusters of hard spheres in spherical confinement. *Nat. Phys.* **2021**, *17*, 128–134.

[80] Wang, D.; Hermes, M.; Najmr, S.; Tasios, N.; Grau-Carbonell, A.; Liu, Y.; Bals, S.; Dijkstra, M.; Murray, C. B.; van Blaaderen, A. Structural diversity in three-dimensional self-assembly of nanoplatelets by spherical confinement. *Nat. Commun.* **2022**, *13*, 6001.

[81] Yang, Y.; Wang, Y. L.; Jin, S. M.; Xu, J. P.; Hou, Z. Y.; Ren, J. L.; Wang, K.; Lee, E.; Zhang, L. B.; Zhang, Y. F. et al. 3D confined assembly of polymer-tethered gold nanoparticles into size-segregated structures. *Mater*. Chem. *Front.* **2019**, *3*, 209–215.

[82] Cantoni, M.; Holzer, L. Advances in 3D focused ion beam tomography. *MRS Bull.* **2014**, *39*, 354–360.

[83] Hamon, C.; Sanz-Ortiz, M. N.; Modin, E.; Hill, E. H.; Scarabelli, L.; Chuvilin, A.; Liz-Marzan, L. M. Hierarchical organization and molecular diffusion in gold nanorod/silica supercrystal nanocomposites. *Nanoscale* **2016**, *8*, 7914–7922.

[84] van der Hoeven, J. E. S.; van der Wee, E. B.; de Winter, D. A. M.; Hermes, M.; Liu, Y.; Fokkema, J.; Bransen, M.; van Huis, M. A.; Gerritsen, H. C.; de Jongh, P. E. et al. Bridging the gap: 3D real-space characterization of colloidal assemblies via FIB-SEM tomography. *Nanoscale* **2019**, *11*, 5304–5316.

[85] Wang, Y.; Chen, J.; Li, R. P.; Götz, A.; Drobek, D.; Przybilla, T.; Hübner, S.; Pelz, P.; Yang, L.; Apeleo Zubiri, B. et al. Controlled self-assembly of gold nanotetrahedra into quasicrystals and complex periodic supracrystals. *J. Am. Chem. Soc.* **2023**, *145*, 17902–17911.

[86] Ophus, C. Four-dimensional scanning transmission electron microscopy (4D-STEM): From scanning nanodiffraction to ptychography and beyond. *Microsc. Microanal.* **2019**, *25*, 563–582.

[87] Savitzky, B. H.; Zeltmann, S. E.; Hughes, L. A.; Brown, H. G.; Zhao, S. T.; Pelz, P. M.; Pekin, T. C.; Barnard, E. S.; Donohue, J.; Rangel DaCosta, L. et al. py4DSTEM: A software package for four-dimensional scanning transmission electron microscopy data analysis. *Microsc. Microanal.* **2021**, *27*, 712–743.

[88] Johnstone, D.; Crout, P.; Nord, M.; Francis, C.; Laulainen, J.; Høgås, S.; Opheim, E.; Martineau, B.; Bergh, T.; Prestat, E. et al. pyxem/pyxem: Pyxem 0.14.2. 2022. https://doi.org/10.5281/ZENODO.6645923.

[89] daSilva, J. C.; Smeaton, M. A.; Dunbar, T. A.; Xu, Y. Z.; Balazs, D. M.; Kourkoutis, L. F.; Hanrath, T. Mechanistic insights into superlattice transformation at a single nanocrystal level using nanobeam electron diffraction. *Nano Lett.* **2020**, *20*, 5267–5274.

[90] De Yoreo, J. J.; Sommerdijk, N. A. J. M. Investigating materials formation with liquid-phase and cryogenic TEM. *Nat. Rev. Mater*. **2016**, *1*, 16035.

[91] Patterson, J. P.; Xu, Y. F.; Moradi, M. A.; Sommerdijk, N. A. J. M.; Friedrich, H. CryoTEM as an advanced analytical tool for materials chemists. *Acc. Chem. Res.* **2017**, *50*, 1495–1501.

[92] Watt, J.; Huber, D. L.; Stewart, P. L. Soft matter and nanomaterials characterization by cryogenic transmission electron microscopy. *MRS Bull.* **2019**, *44*, 942–948.

[93] Kostiainen, M. A.; Hiekkataipale, P.; Laiho, A.; Lemieux, V.; Seitsonen, J.; Ruokolainen, J.; Ceci, P. Electrostatic assembly of binary nanoparticle superlattices using protein cages. *Nat. Nanotechnol.* **2012**, *8*, 52–56.

[94] Walker, D. A.; Leitsch, E. K.; Nap, R. J.; Szleifer, I.; Grzybowski, B. A. Geometric curvature controls the chemical patchiness and self-assembly of nanoparticles. *Nat. Nanotechnol.* **2013**, *8*, 676–681.

[95] Koneti, S.; Roiban, L.; Dalmas, F.; Langlois, C.; Gay, A. S.; Cabiac, A.; Grenier, T.; Banjak, H.; Maxim, V.; Epicier, T. Fast electron tomography: Applications to beam sensitive samples and *in situ* TEM or *operando* environmental TEM studies. *Mater. Charact.* **2019**, *151*, 480–495.

[96] Albrecht, W.; Bals, S. Fast electron tomography for nanomaterials. *J. Phys. Chem. C* **2020**, *124*, 27276–27286.

[97] Vanrompay, H.; Skorikov, A.; Bladt, E.; Béché, A.; Freitag, B.; Verbeeck, J.; Bals, S. Fast versus conventional HAADF-STEM tomography of nanoparticles: Advantages and challenges. *Ultramicroscopy* **2021**, *221*, 113191.

[98] Arenas Esteban, D.; Wang, D.; Kadu, A.; Olluyn, N.; Sánchez-Iglesias, A.; Gomez-Perez, A.; González-Casablanca, J.; Nicolopoulos, S.; Liz-Marzán, L. M.; Bals, S. Quantitative 3D structural analysis of small colloidal assemblies under native conditions by liquid-cell fast electron tomography. *Nat. Commun.* **2024**, *15*, 6399.

[99] Park, J.; Zheng, H. M.; Lee, W. C.; Geissler, P. L.; Rabani, E.; Alivisatos, A. P. Direct observation of nanoparticle superlattice formation by using liquid cell transmission electron microscopy. *ACS Nano* **2012**, *6*, 2078–2085.

[100] Liu, Y. Z.; Lin, X. M.; Sun, Y. G.; Rajh, T. *In situ* visualization of self-assembly of charged gold nanoparticles. *J. Am. Chem. Soc.* **2013**, *135*, 3764–3767.

[101] Ross, F. M. Opportunities and challenges in liquid cell electron microscopy. *Science* **2015**, *350*, aaa9886.

[102] Woehl, T. J.; Prozorov, T. The mechanisms for nanoparticle surface diffusion and chain self-assembly determined from real-time nanoscale kinetics in liquid. *J. Phys. Chem. C* **2015**, *119*, 21261–21269.

[103] Sutter, E.; Sutter, P.; Tkachenko, A. V.; Krahne, R.; de Graaf, J.; Arciniegas, M.; Manna, L. *In situ* microscopy of the self-assembly of branched nanocrystals in solution. *Nat. Commun.* **2016**, *7*, 11213.

[104] Miele, E.; Raj, S.; Baraissov, Z.; Kral, P.; Mirsaidov, U. Dynamics of

templated assembly of nanoparticle filaments within nanochannels. *Adv. Mater.* **2017**, *29*, 1702682.

[105] Powers, A. S.; Liao, H. G.; Raja, S. N.; Bronstein, N. D.; Alivisatos, A. P.; Zheng, H. M. Tracking nanoparticle diffusion and interaction during self-assembly in a liquid cell. *Nano Lett.* **2017**, *17*, 15–20.

[106] Lee, J.; Nakouzi, E.; Song, M.; Wang, B.; Chun, J.; Li, D. S. Mechanistic understanding of the growth kinetics and dynamics of nanoparticle superlattices by coupling interparticle forces from real-time measurements. *ACS Nano* **2018**, *12*, 12778–12787.

[107] Ou, Z. H.; Wang, Z. W.; Luo, B. B.; Luijten, E.; Chen, Q. Kinetic pathways of crystallization at the nanoscale. *Nat. Mater.* **2020**, *19*, 450–455.

[108] Cepeda-Perez, E.; Doblas, D.; Kraus, T.; de Jonge, N. Electron microscopy of nanoparticle superlattice formation at a solid-liquid interface in nonpolar liquids. *Sci. Adv.* **2020**, *6*, eaba1404.

[109] Chen, Q.; Yuk, J. M.; Hauwiller, M. R.; Park, J.; Dae, K. S.; Kim, J. S.; Alivisatos, A. P. Nucleation, growth, and superlattice formation of nanocrystals observed in liquid cell transmission electron microscopy. *MRS Bull.* **2020**, *45*, 713–726.

[110] Mirsaidov, U.; Patterson, J. P.; Zheng, H. M. Liquid phase transmission electron microscopy for imaging of nanoscale processes in solution. *MRS Bull.* **2020**, *45*, 704–712.

[111] Woehl, T. J.; Moser, T.; Evans, J. E.; Ross, F. M. Electron-beam-driven chemical processes during liquid phase transmission electron microscopy. *MRS Bull.* **2020**, *45*, 746–753.

[112] Zhong, Y. X.; Allen, V. R.; Chen, J.; Wang, Y.; Ye, X. C. Multistep crystallization of dynamic nanoparticle superlattices in nonaqueous solutions. *J. Am. Chem. Soc.* **2022**, *144*, 14915–14922.

[113] Li, D. S.; Chen, Q.; Chun, J.; Fichthorn, K.; De Yoreo, J.; Zheng, H. M. Nanoparticle assembly and oriented attachment: Correlating controlling factors to the resulting structures. *Chem. Rev.* **2023**, *123*, 3127–3159.

[114] Zhong, Y. X.; Moore, T. C.; Dwyer, T.; Butrum-Griffith, A.; Allen, V. R.; Chen, J.; Wang, Y.; Cheng, F. R.; Glotzer, S. C.; Ye, X. C. Engineering and direct imaging of nanocube self-assembly pathways. *Nat. Chem. Eng.* **2024**, *1*, 532–541.

[115] Kim, J.; Kang, S.; Cheng, F. R.; Wang, Y.; Ye, X. C.; Park, J. Recent advances in liquid phase transmission electron microscopy of nanoparticle growth and self-assembly. *MRS Bull.* **2024**, *49*, 365–376.

[116] Ronneberger, O.; Fischer, P.; Brox, T. U-Net: Convolutional networks for biomedical image segmentation. In *Proceedings of the 18th International Conference on Medical Image Computing and Computer-Assisted Intervention*, Munich, Germany, 2015, pp 234–241.

[117] Horwath, J. P.; Zakharov, D. N.; Mégret, R.; Stach, E. A. Understanding important features of deep learning models for segmentation of high-resolution transmission electron microscopy images. *npj Comput. Mater.* **2020**, *6*, 108.

[118] Yao, L. H.; Ou, Z. H.; Luo, B. B.; Xu, C.; Chen, Q. Machine learning to reveal nanoparticle dynamics from liquid-phase tem videos. *ACS Cent. Sci.* **2020**, *6*, 1421–1430.

[119] Ede, J. M. Deep learning in electron microscopy. *Mach. Learn.: Sci. Technol.* **2021**, *2*, 011004.

[120] Spurgeon, S. R.; Ophus, C.; Jones, L.; Petford-Long, A.; Kalinin, S. V.; Olszta, M. J.; Dunin-Borkowski, R. E.; Salmon, N.; Hattar, K.; Yang, W. C. D. et al. Towards data-driven next-generation transmission electron microscopy. *Nat. Mater.* **2021**, *20*, 274–279.

[121] Lin, R. Q.; Zhang, R.; Wang, C. Y.; Yang, X. Q.; Xin, H. L. TEMImageNet training library and AtomSegNet deep-learning models for high-precision atom segmentation, localization, denoising, and deblurring of atomic-resolution images. *Sci. Rep.* **2021**, *11*, 5386.